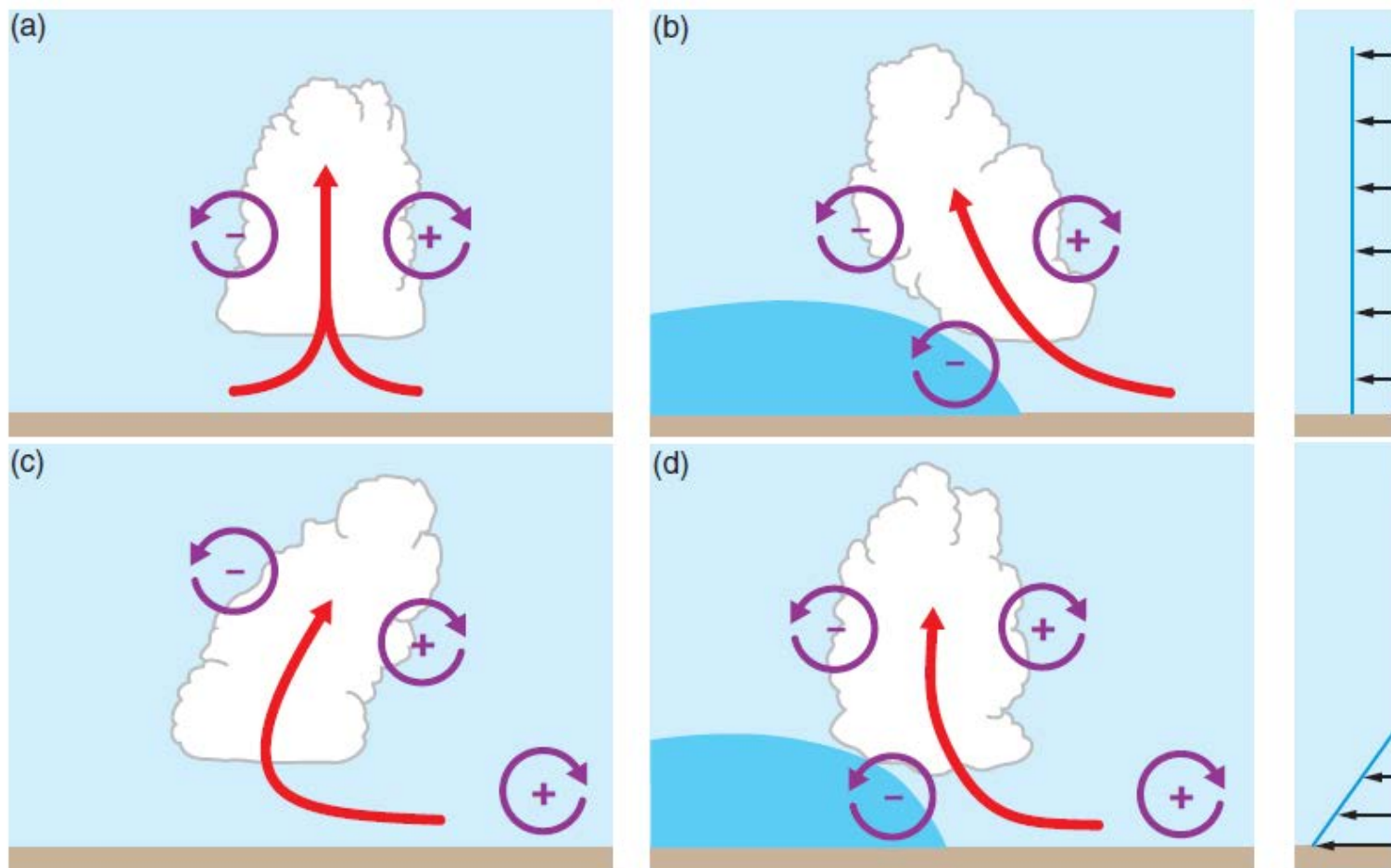# RKW theory

Optimal condition $\quad \Delta u = c$

- Δu is line-normal vertical shear over 0-2.5km

- C is the theoretical gust front speed, which is the square of twice the integration of buoyancy in the cold pool over the depth of the cold pool.
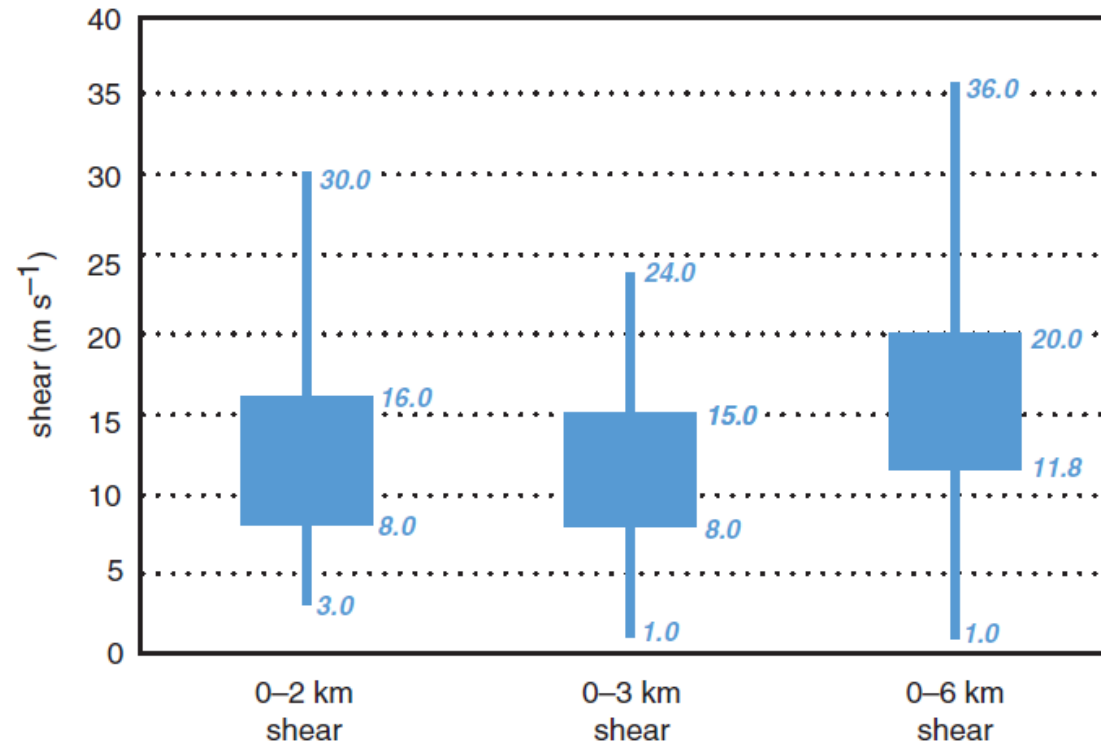
$$-2 \int_0^H B_L \, dz = c^2$$

For most thunderstorm outflows, RKW theory implies an optimal shear of 17-25 m/s over 0-2.5km layer.

Controversy about RKW theory

- Shear vs. Severity : the vertical shear is significantly weaker than required by RKW for many **strong-wind producing** squall lines
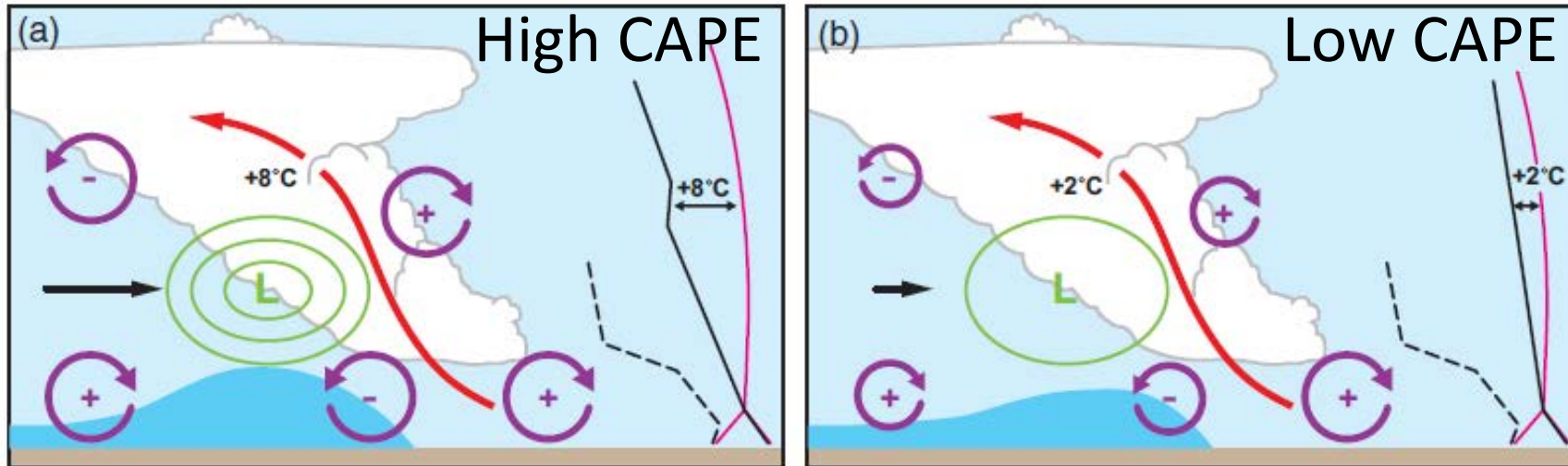
RI: formation

上节课回顾

$$p' \propto \underbrace{\underbrace{\left[\left(\frac{\partial u'}{\partial x}\right)^2 + \left(\frac{\partial v'}{\partial y}\right)^2 + \left(\frac{\partial w'}{\partial z}\right)^2\right]}_{\text{fluid extension terms}} \underbrace{-\frac{1}{2}\zeta'^2}_{\text{spin term}}}_{\text{nonlinear dynamic pressure perturbation, } p'_{dnl}}$$

Aspect 1: Mid-level pressure deficit

as a result of $\partial B/\partial z > 0$

$$+ \underbrace{2\mathbf{S}\cdot\boldsymbol{\nabla}_h w'}_{\substack{\text{linear dynamic pressure} \\ \text{perturbation, } p'_{dl}}} \qquad \underbrace{-\frac{\partial B}{\partial z}}_{\substack{\text{buoyancy pressure perturbation, } p'_b}}. \qquad (8.24)$$

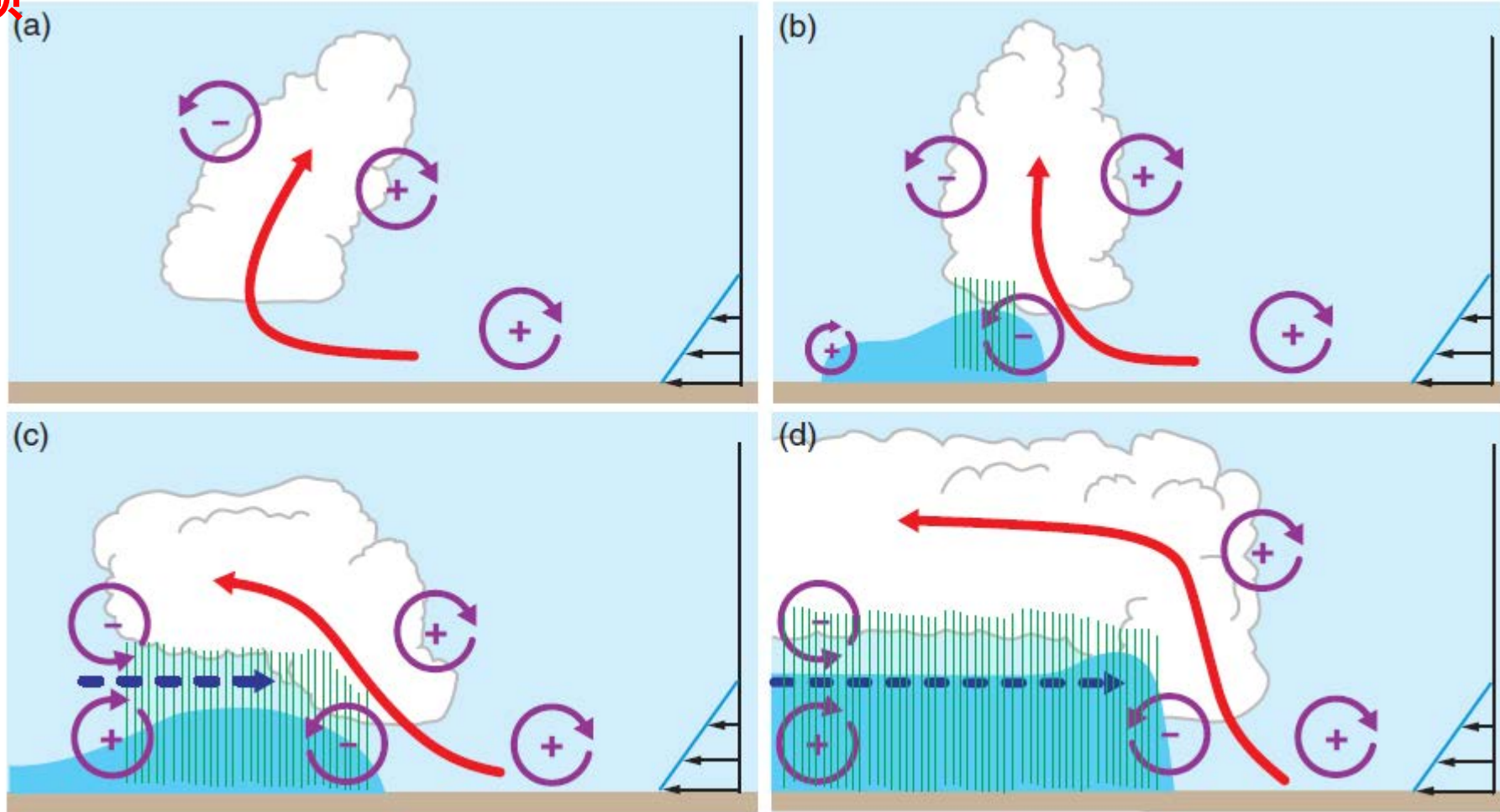Aspect 2: Vorticity couplets at the rear of the cold pool

RI impact on the updraft
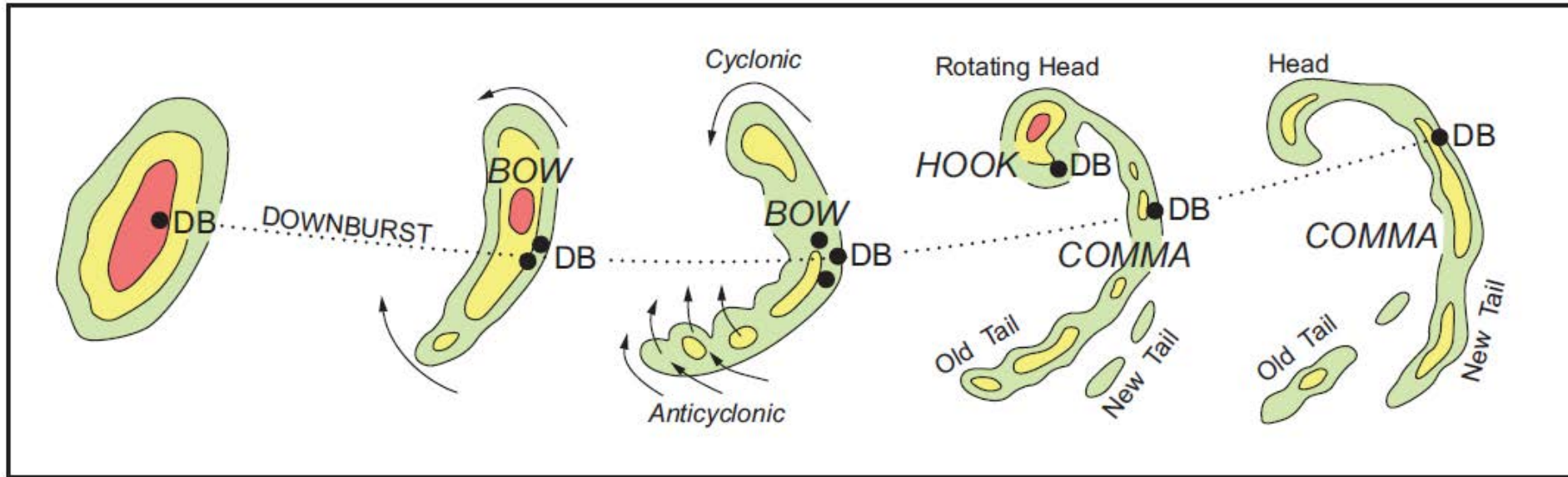
$$\Delta u^2 + \Delta u_j^2 = c^2,$$
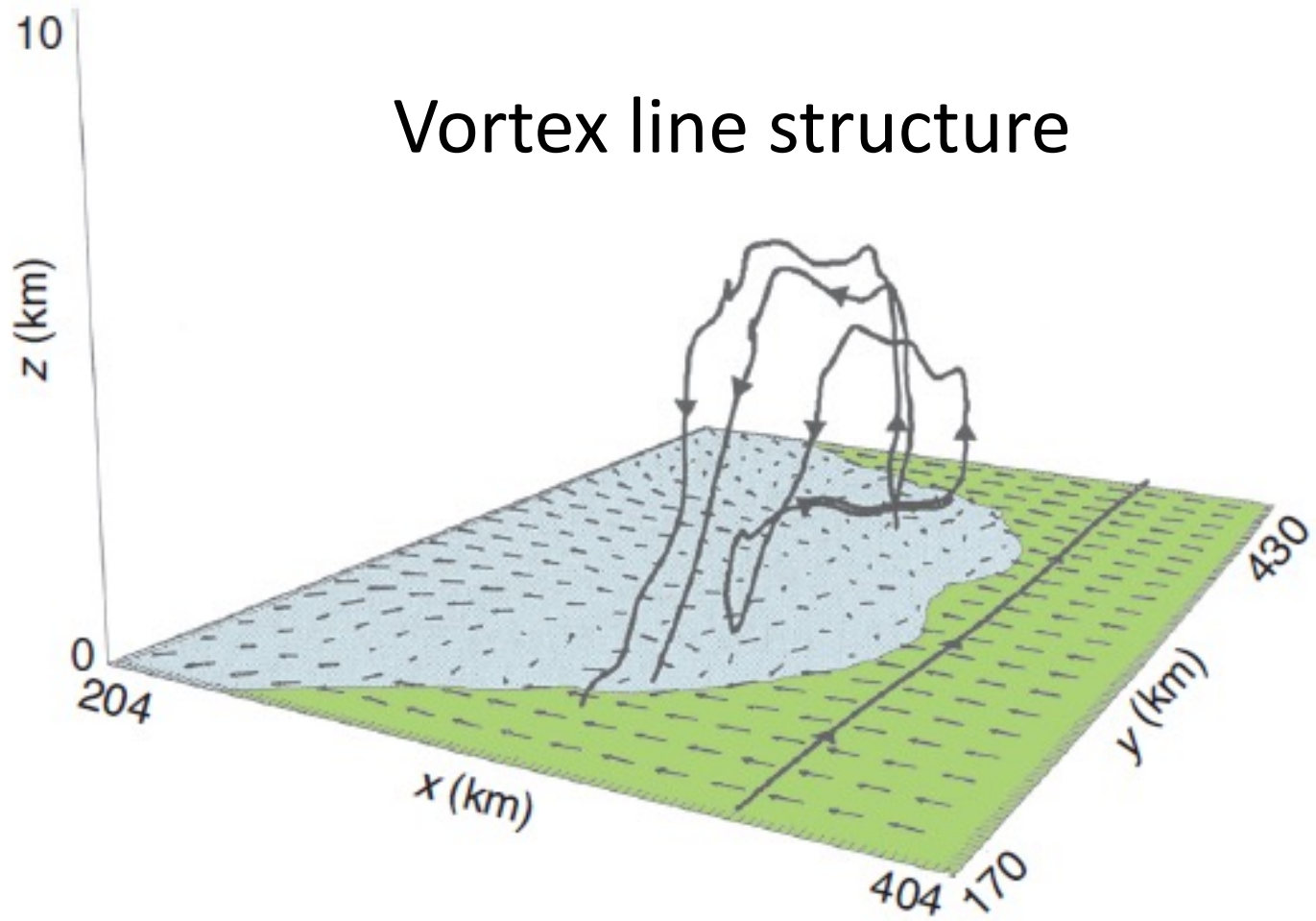
Bow Echo

Figure 9.24 Fujita's conceptual model of a bow echo. Black dots labeled 'DB' are downburst locations. Colors are radar echo intensity. (Adapted from Fujita [1978].)
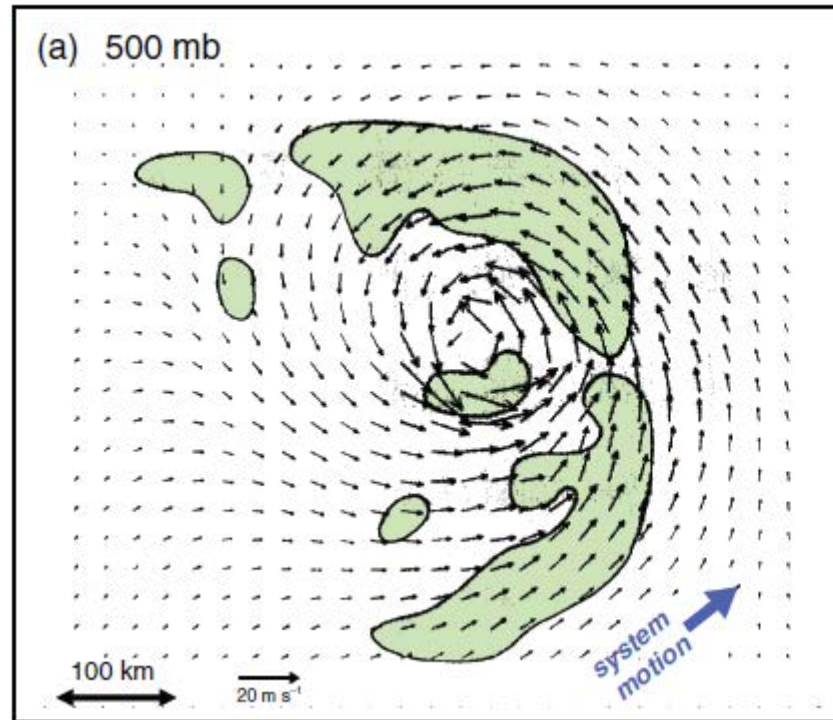
Rear inflow

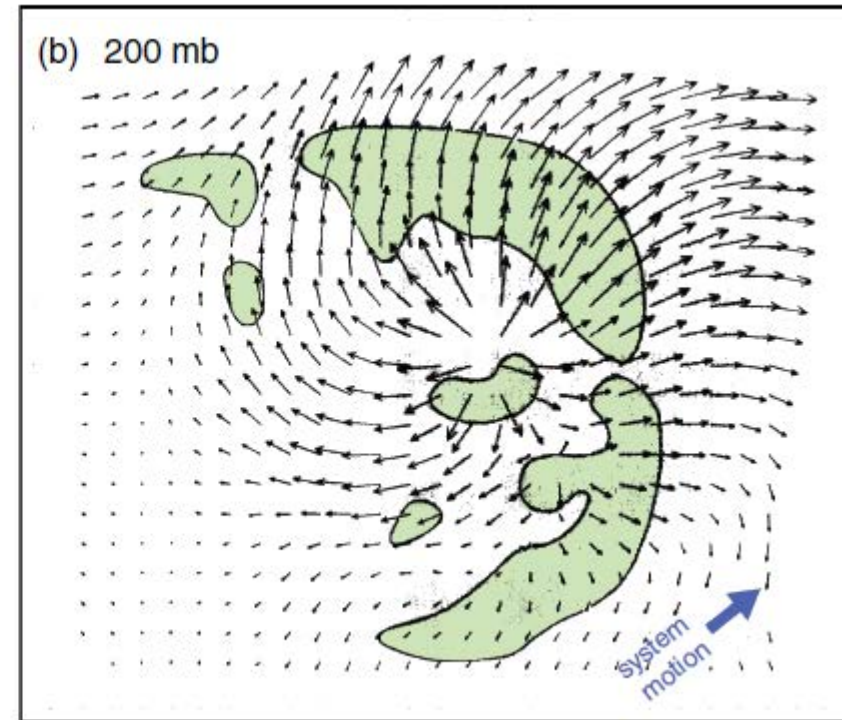Line-end vortices Bookend vortices

Formation of line End Vortices:

Vortex line structure

Structure

MCCs generate warm core meso-α-scale circulation

MCV

Mesohigh
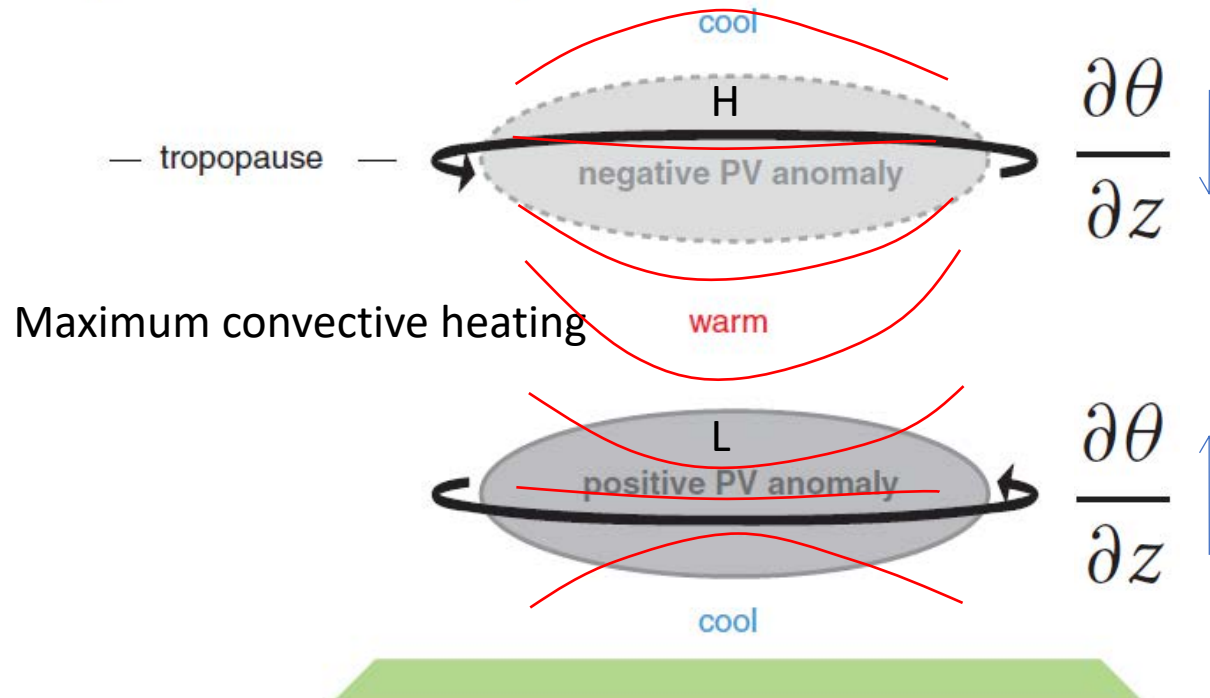
Formation of the cyclonic & anticyclonic circulation

Ertel PV theorem

• Potential vorticity anomalies

$$\frac{d}{dt}\left\{\frac{\omega_a}{\rho}\cdot\nabla\lambda\right\} = \frac{\omega_a}{\rho}\cdot\nabla\Psi + \nabla\lambda\cdot\left[\frac{\nabla\rho\times\nabla p}{\rho^3}\right] + \frac{\nabla\lambda}{\rho}\cdot\left\{\nabla\times\frac{\mathscr{F}}{\rho}\right\}.$$

$$PV = \frac{(\boldsymbol{\omega}+f\mathbf{k})\cdot\nabla\theta}{\rho} \approx \frac{\zeta+f}{\rho}\frac{\partial\theta}{\partial z}$$

cool

H

— tropopause —

negative PV anomaly

$$\frac{\partial\theta}{\partial z}$$

Maximum convective heating
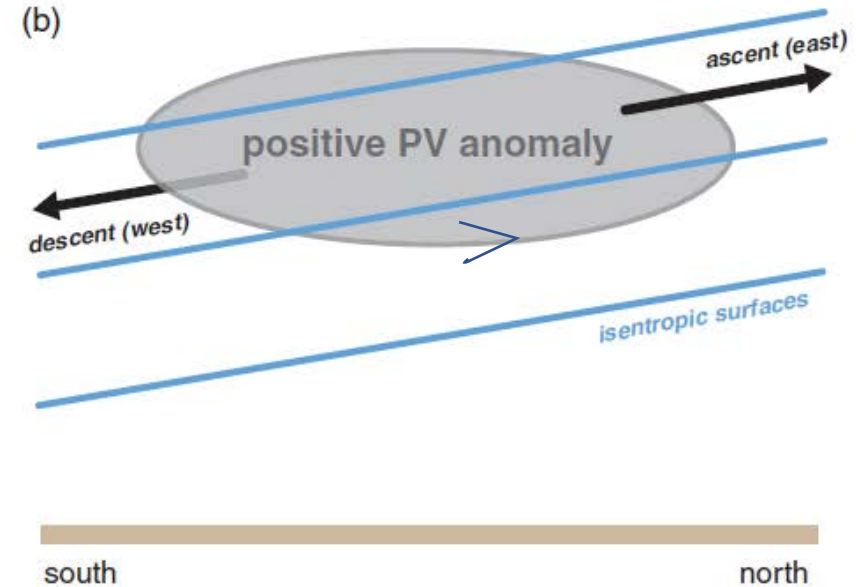
warm

L

positive PV anomaly

$$\frac{\partial\theta}{\partial z}$$

cool

Maintenance of MCC

- PV thinking
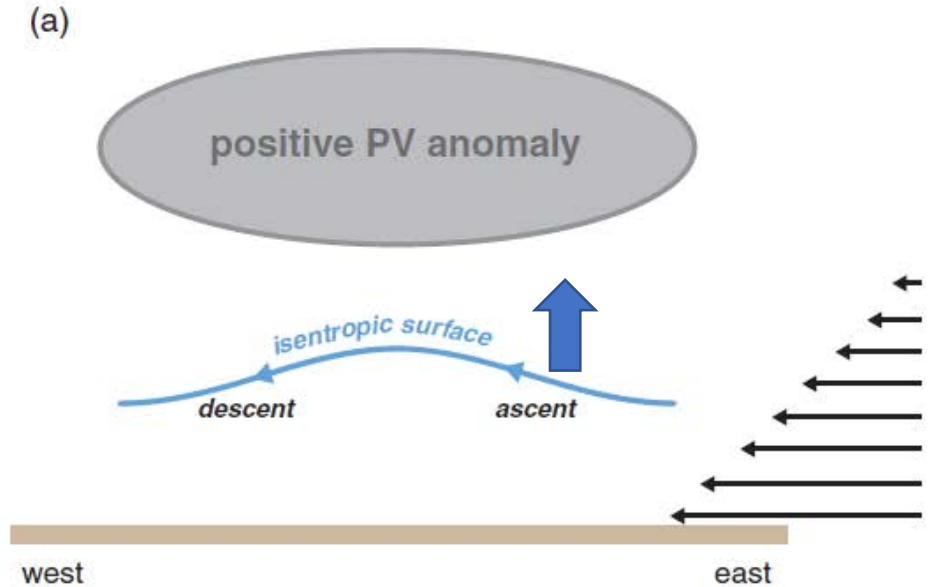
Vertical shear⟶Thermal Wind⟶tilted isotropic surface
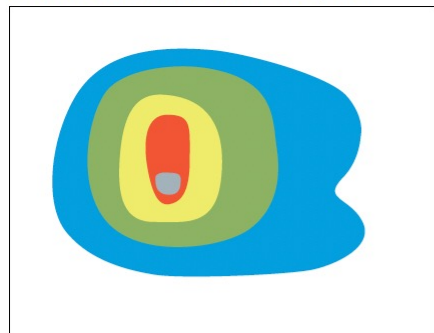
4.3 中尺度对流系统的前沿进展：观测

The formation, character and changing nature of mesoscale convective systems

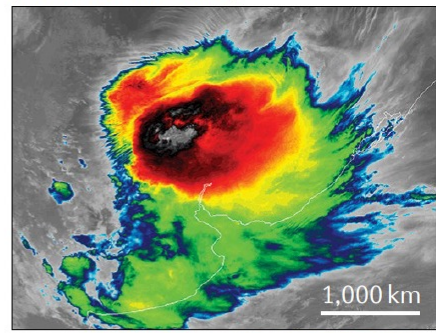*Russ S. Schumacher* (iD) ✉ *and Kristen L. Rasmussen*

Abstract | Mesoscale convective systems (MCSs) describe organized groupings of thunderstorms in the tropics and mid-latitudes that span thousands of square kilometres. While recognized for over a century, the advent of satellite and radar observations, as well as atmospheric-model simulations, has brought about their increased understanding. In this Review, we synthesize current knowledge on MCS formation, climatological characteristics, hazardous weather, predictive capacity and projected changes with anthropogenic warming. Driven by typical deep moist convective processes (moisture, lift and instability) and vertical wind shear, MCS formation occurs preferentially in locations where these ingredients are present and can be maintained by large-scale ascent and the cold pools that they produce. MCSs also generate hazardous weather, including extreme rainfall, flooding, derechos and, sometimes, tornadoes and hail, all of which have substantial economic and societal impacts. Given that MCSs also produce a large fraction of warm-season rainfall, there is critical need for both short-term forecasts and long-term projections, presently challenged by inadequate model resolution. Yet, with continually improving modelling capabilities, as well as greater theoretical basis, it is suggested that MCSs might increase in frequency and intensity under a warming climate. Further modelling progress, in turn, offers improved understanding of MCS characteristics, from their life cycle through to impacts.
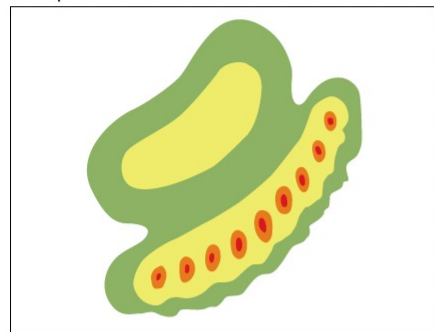
a Mesoscale convective complex — (12 November 2019)

Temp (°C): 50 30 10 0 −10 −30 −50 −70 −90

b Squall line — (13 July 2015)

c Bow echo — (20 August 2019)
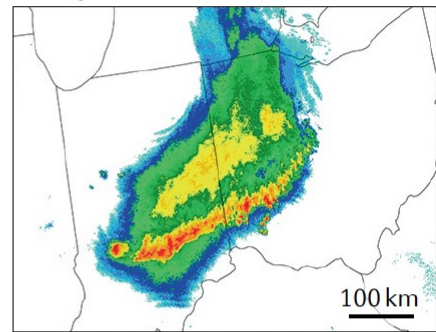
Reflectivity (dBZ): 0 10 20 30 40 50 60 70

d Training line/adjoining stratiform — (4 June 2014)
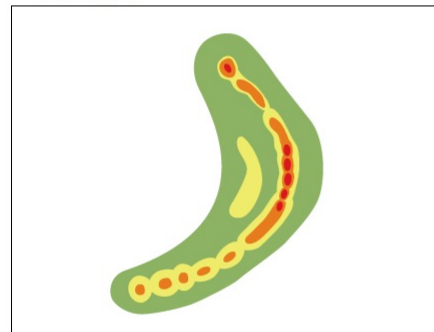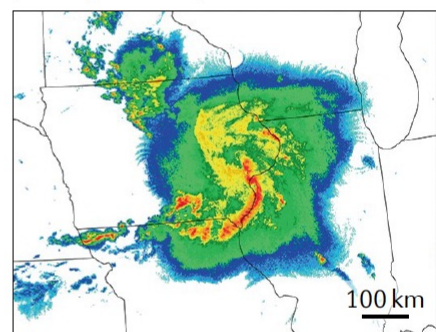
e Back-building/quasistationary — (16 July 2019)

Fig. 1 | **Key MCS types.** Schematic illustration (left) and observed infrared or radar retrievals (right) of a mesoscale convective complex (panel **a**), squall line (panel **b**), bow echo (panel **c**), training line/adjoining stratiform mesoscale convective system (MCS; panel **d**) and back-building MCS (panel **e**). Radar data in panels **b**–**e** are from the Multi-Radar Multi-Sensor system[183]. MCSs can take on a wide variety of structures, with the examples shown here among the most highly organized. Schematics in panels **d** and **e** adapted with permission from REF.[5], © American Meteorological Society.

a MCS contribution to total rainfall
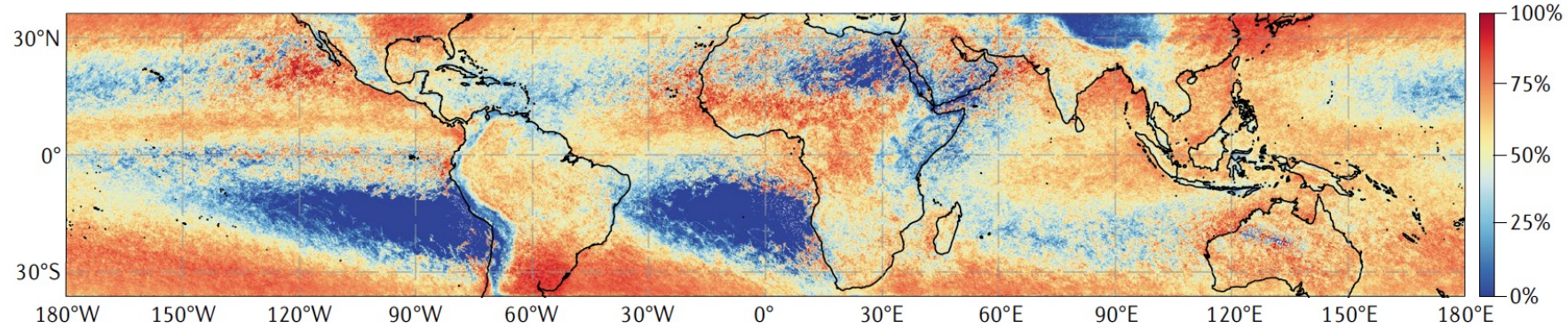
b Diurnal cycle: land

c Diurnal cycle: ocean

MCS Large mid-level Shallow Small cold Small mid-level
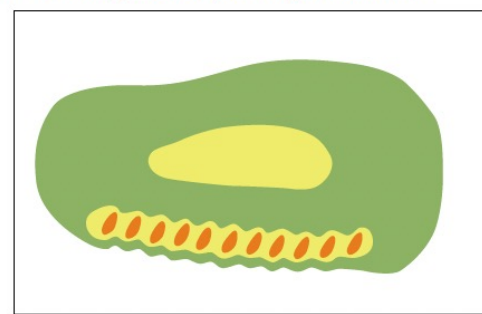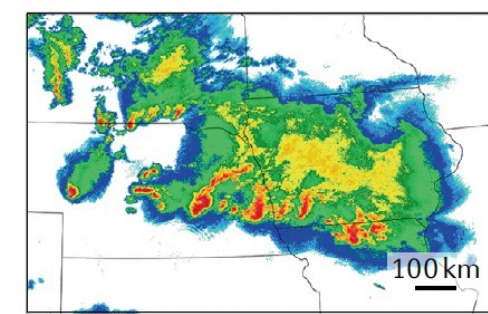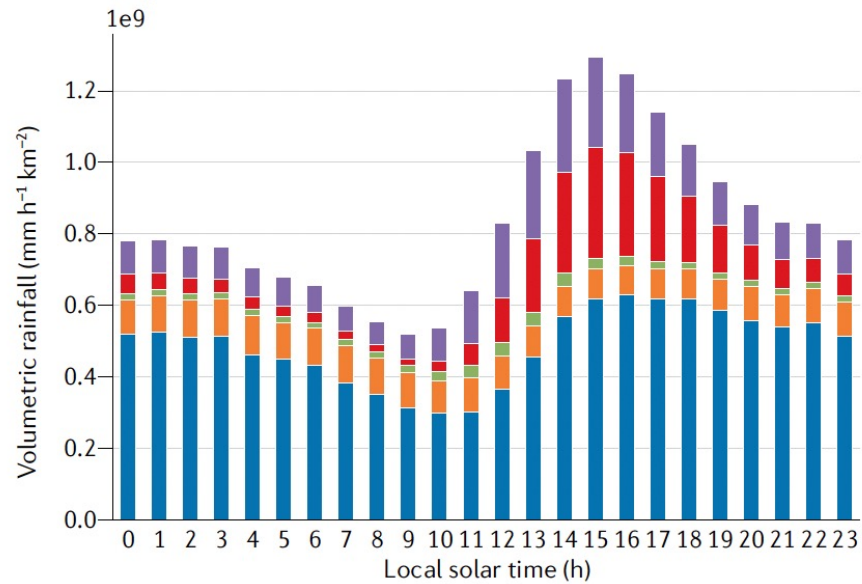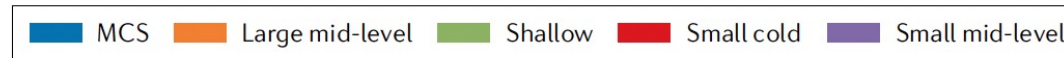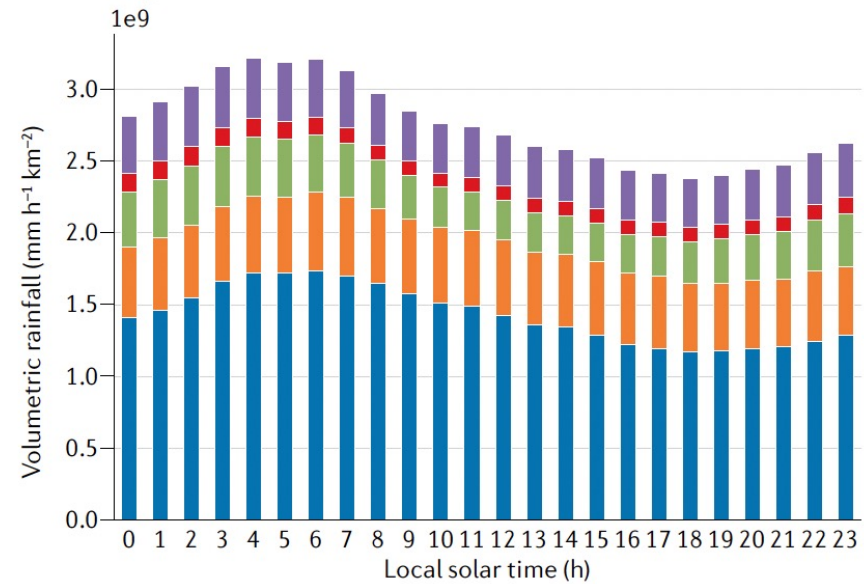
Fig. 2 | **The contribution of MCSs to global rainfall.** Fraction of annual rainfall produced by mesoscale convective systems (MCSs) based on observations from the Tropical Rainfall Measuring Mission (TRMM) satellite between December 1997 and September 2014 (panel **a**). Diurnal cycle of TRMM volumetric rainfall over the land (panel **b**) and ocean (panel **c**) between 36°N/S. In many parts of the global tropics, subtropics and mid-latitudes, MCSs produce a large fraction of the annual precipitation. MCSs over land have a strong diurnal cycle, with rain maximized in the afternoon and evening, and minimized in the morning; MCSs over ocean have a less pronounced diurnal cycle. Panel **a** adapted with permission from REF.[6], © American Meteorological Society. Panels **b** and **c** adapted with permission from REF.[50], © American Meteorological Society.
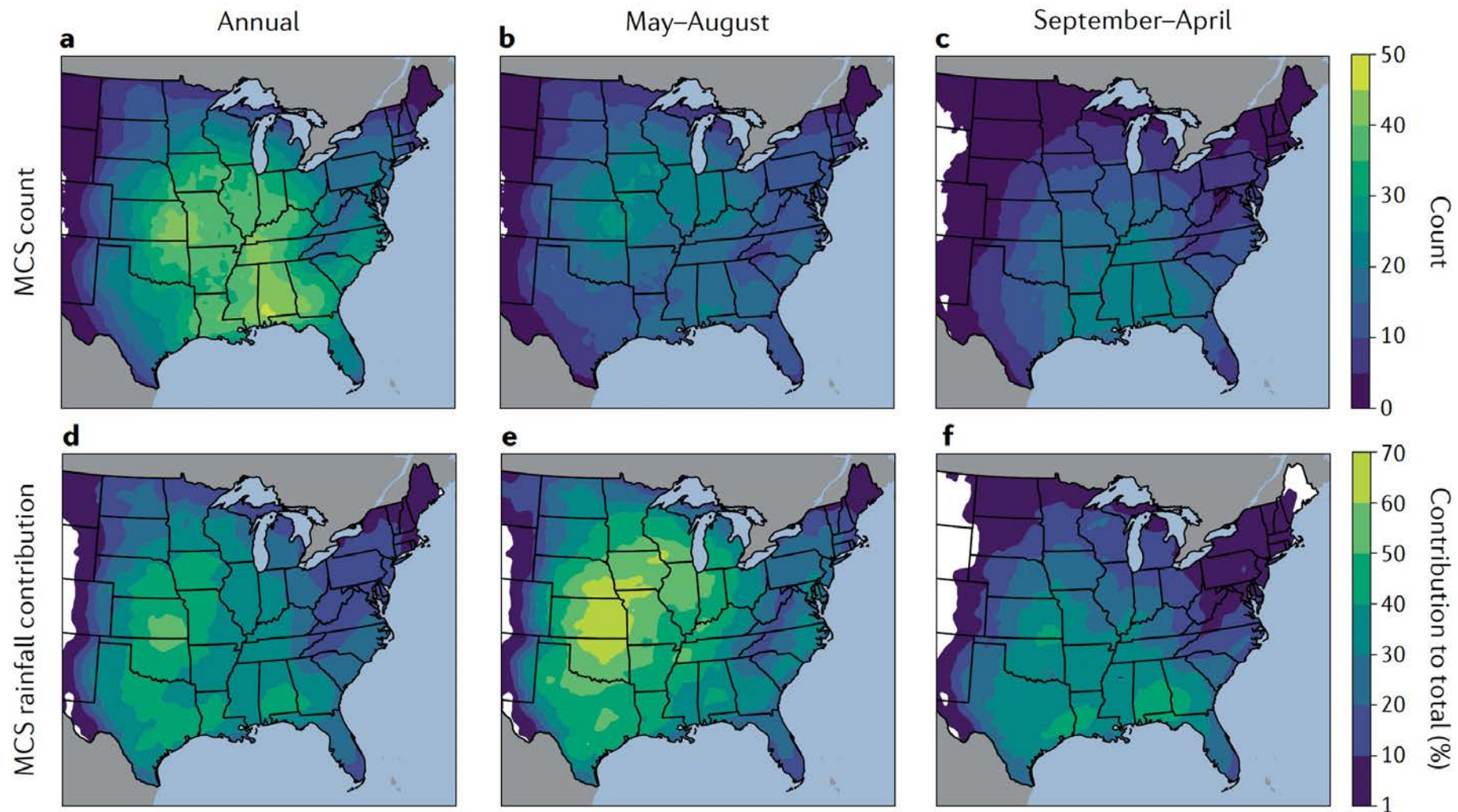
Fig. 3 | **MCS frequency and the rainfall contribution of MCSs in the USA.** Mean mesoscale convective system (MCS) occurrence over the USA for January–December (panel **a**), May–August (panel **b**) and September–April (panel **c**). Percentage contribution of MCS rainfall to total rainfall for January–December (panel **d**), May–August (panel **e**) and September–April (panel **f**). Over the USA, where there is a long record of radar and precipitation data, MCSs are found to be frequent and to contribute over half of the annual rainfall in the agriculturally productive central USA. Adapted with permission from REF.[7], © American Meteorological Society.

a Translating cold front pattern

500 hPa

Surface

500 km
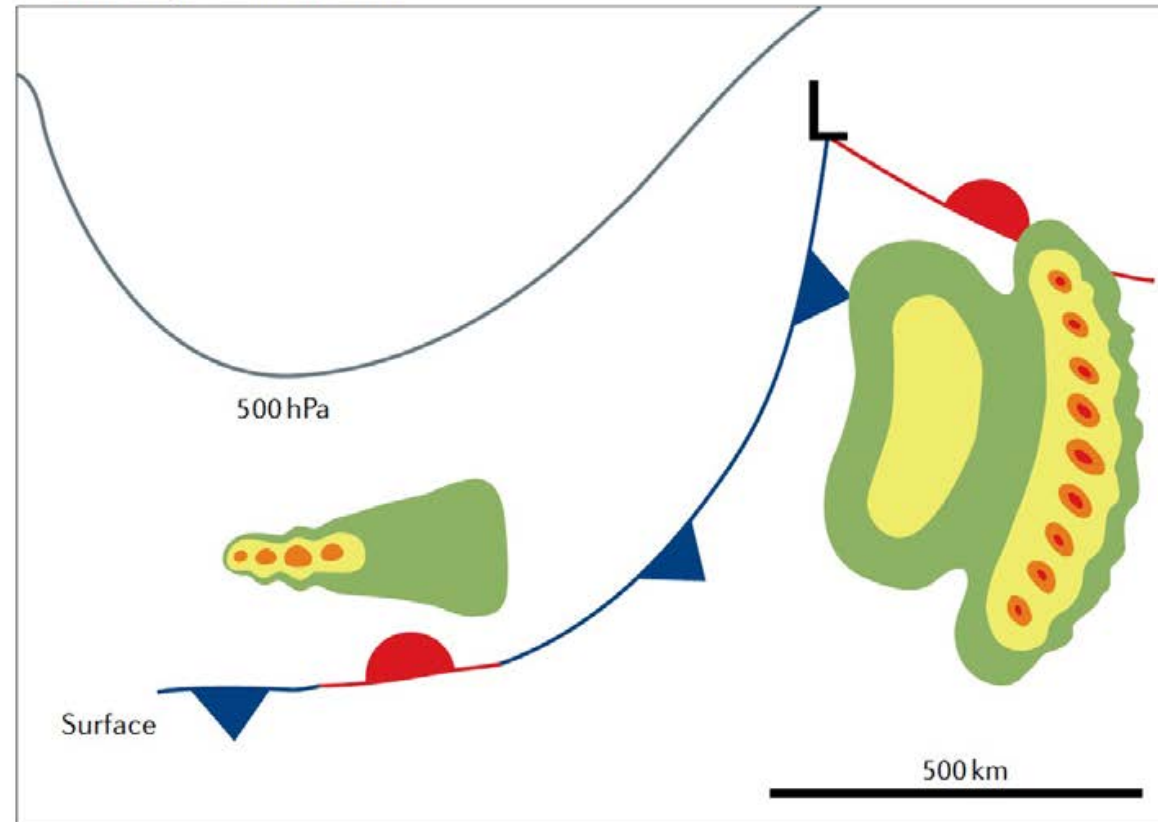
b Quasistationary east–west front pattern

500 hPa

Surface

500 km
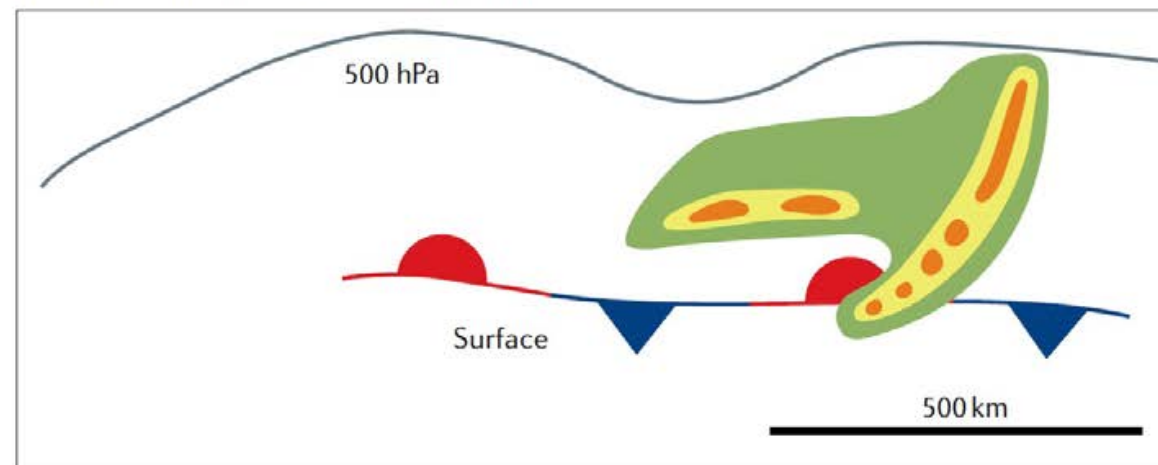
Fig. 4 | **Common environments for MCS formation and maintenance.** Synoptic environments conducive for mesoscale convective system (MCS) formation in a translating cold front (panel **a**) and quasistationary east–west front (panel **b**). Schematics illustrate common MCS types observed in those environments, consistent with the definitions shown in FIG. 1. Solid black lines indicate a 500-hPa geopotential height contour. Red lines with half-circles, blue lines with triangles, and alternating patterns represent warm, cold and stationary surface fronts, respectively. MCSs form in environments where the required ingredients of moisture, instability, lift and vertical wind shear are brought together; these two examples highlight two such common regimes in mid-latitudes. Adapted with permission from REF.[71], © American Meteorological Society.
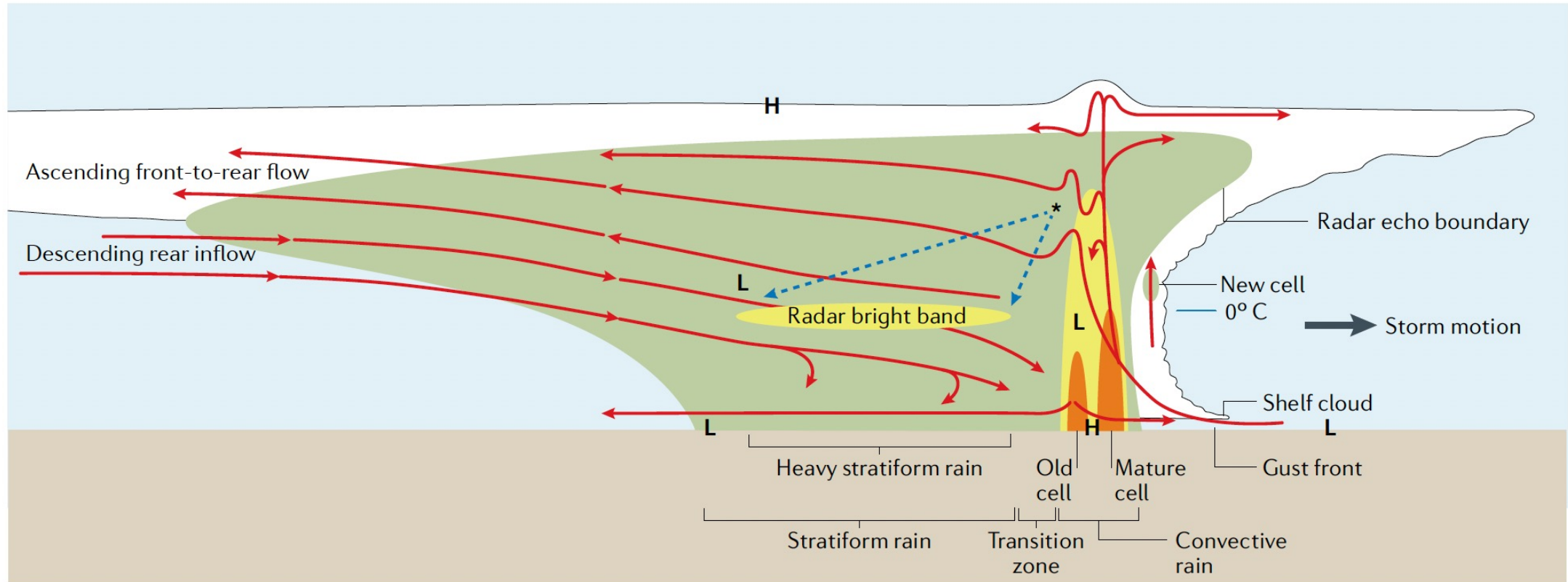
Fig. 5 | Conceptual model of a squall line. The vertical cross section is oriented perpendicular to the convective line, with a trailing stratiform region. The green shading indicates regions where radar echo is present (that is, where precipitation-sized hydrometeors are observed), with yellow and orange representing stronger radar echoes. Pressure minima and maxima are represented by 'L' and 'H', respectively. The height of the melting level is located just above that of the radar bright band, depicted by the black star and dashed blue arrows. Red arrows indicate the airflow within the mesoscale convective system, including ascending flow from front to rear and descent in a rear-inflow jet. Adapted with permission from REF.[90], © American Meteorological Society.

a Two-hourly continuous radar

b Severe wind reports
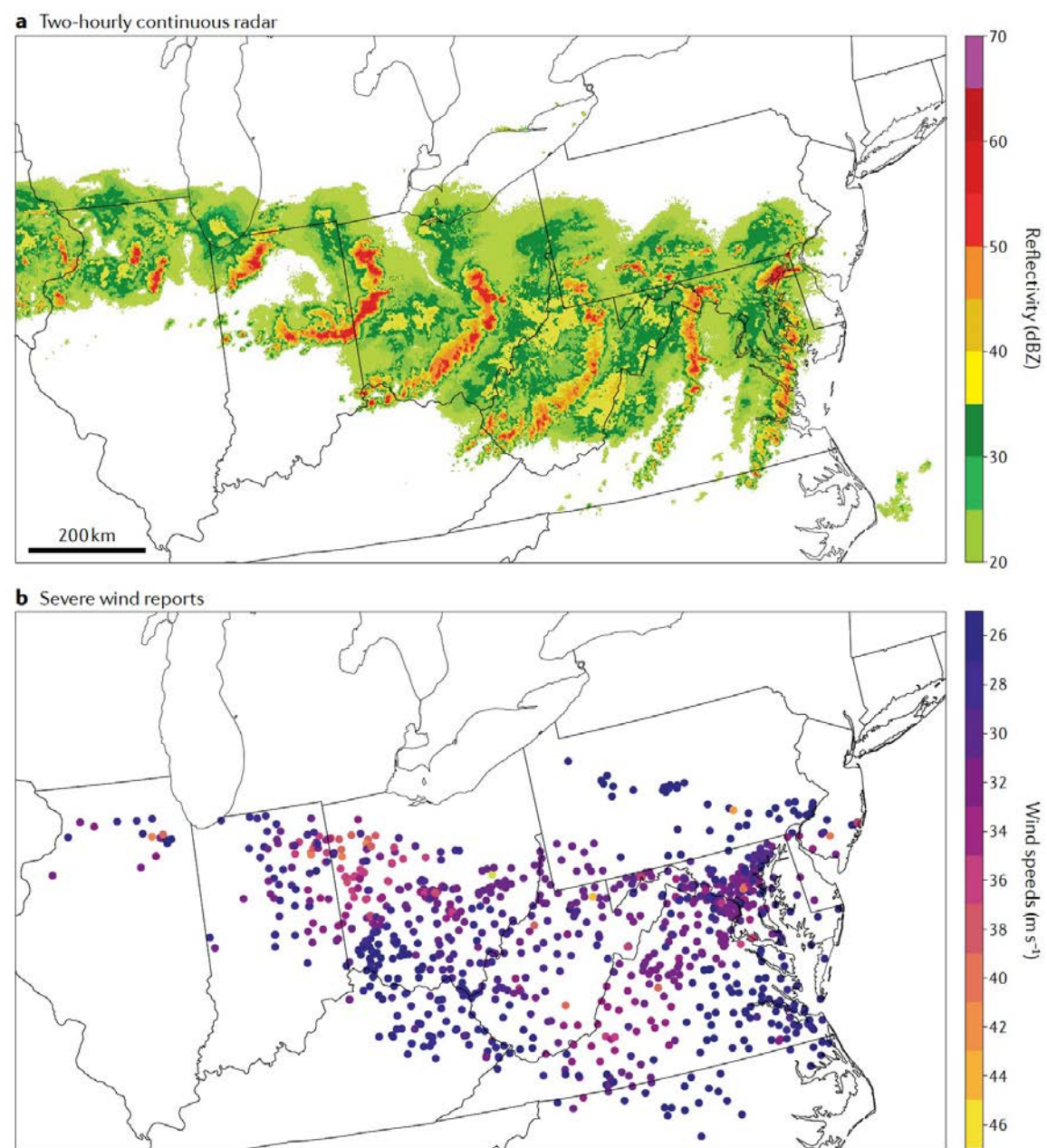
Fig. 6 | **Derecho impacts.** Two-hourly radar continuity map from 1600 UTC 29 June to 0400 UTC 30 June 2012 (panel **a**). Storm Prediction Center severe wind reports for the 29–30 June 2012 progressive derecho (panel **b**). Note that many of the wind speeds contained in the Storm Prediction Center data are estimated. Long-lived bow echoes are capable of producing broad swaths of damaging winds, known as derechos. This event resulted in 22 fatalities and millions of power outages. Radar data in panel **a** from GridRad[184]. Adapted with permission from REF.[106], © American Meteorological Society.

Table 1 | Summary of changes in MCS properties with warming

Variable	Sign of change	Confidence[a]	Refs
MCS characteristics and hazards			
Rainfall (rate and volume)	Increase	High	16–18,119,165, 171,172,185
Severe winds	Uncertain[b]	–	177
Speed of motion	Increase	Low	16
Organization	Uncertain[b]	–	16,17,119,173
Size	Increase	Medium	16,17,119,185
Frequency	Increase	Low	16,165,173
MCS environments			
Atmospheric moisture	Increase	High	14,15,177–181
Atmospheric instability	Increase	High	14,15,177–181
Convective inhibition	Increase	Medium	14,181
Vertical wind shear	Uncertain[b]	–	15,176,178
Frequency of environments supportive of MCSs	Increase	Low	15,17,165, 178,181

MCS, mesoscale convective system. [a]Confidence refers to the convergence of evidence based on different data sources and lines of inquiry. Confidence is rated as high for results that have been consistently found across numerous studies with both theoretical and modelling support. [b]Uncertainty arises owing to inadequate investigation and, as such, there is no estimate of confidence. For MCS organization, there is confidence that changes will occur, but there is uncertainty in what those changes will be, including the sign.

JGR Atmospheres

Key Points:

- Develop an algorithm to track mesoscale convective systems globally using satellite infrared brightness temperature and precipitation data
- Satellite-based tracking reproduces mesoscale convective system statistics derived from tracking using ground-based radar network data

A Global High-Resolution Mesoscale Convective System Database Using Satellite-Derived Cloud Tops, Surface Precipitation, and Tracking

Zhe Feng[1] , L. Ruby Leung[1] , Nana Liu[1] , Jingyu Wang[1] , Robert A. Houze Jr[2], Jianfeng Li[1] , Joseph C. Hardin[1] , Dandan Chen[3], and Jianping Guo[3]

[1]Division of Atmospheric Sciences and Global Change, Pacific Northwest National Laboratory, Richland, WA, USA, [2]Department of Atmospheric Sciences, University of Washington, Seattle, WA, USA, [3]State Key Laboratory of Severe Weather, Chinese Academy of Meteorological Sciences, Beijing, China
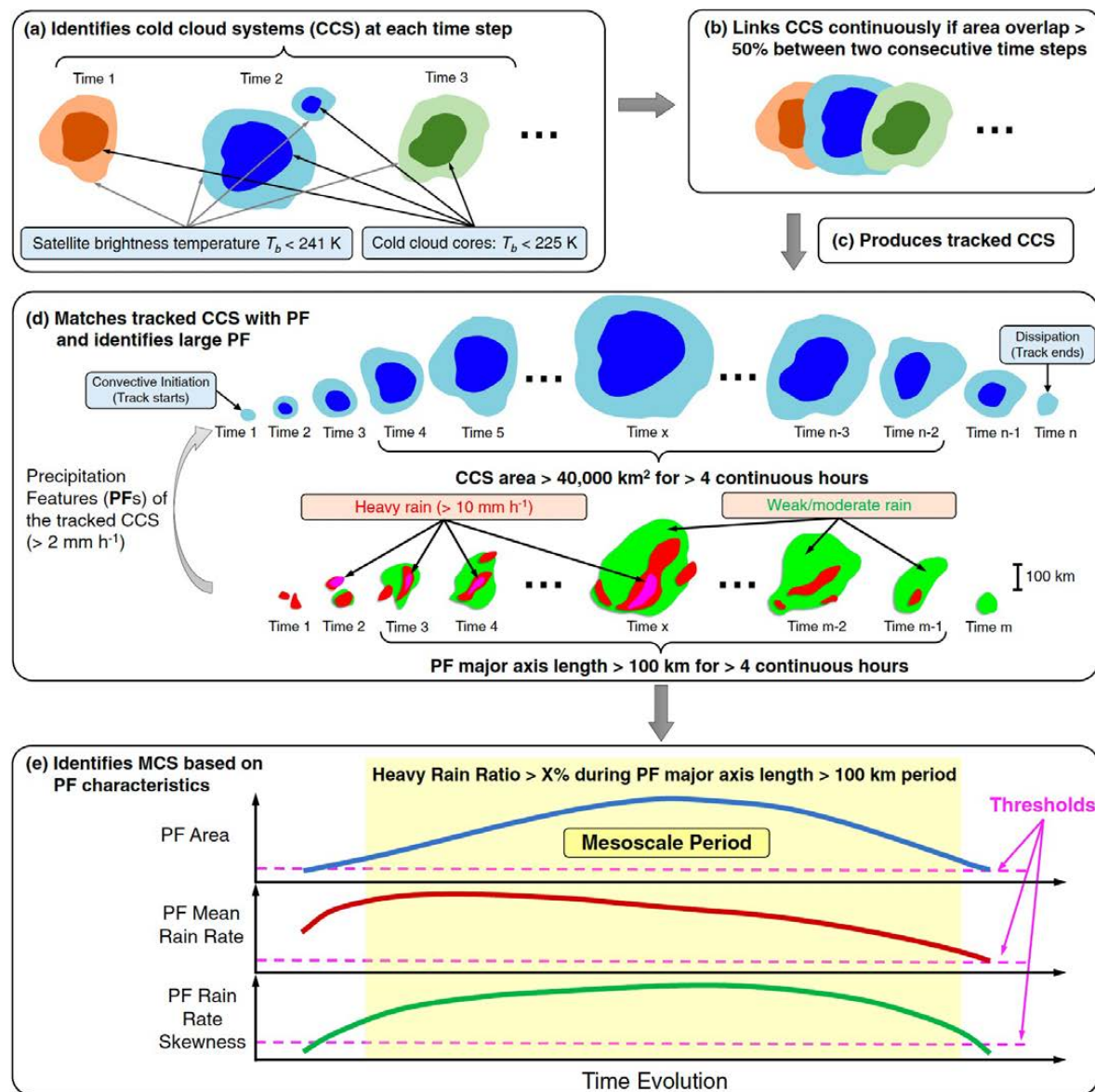
Figure 1. Schematic flowchart of MCS identification using collocated satellite infrared brightness temperature (T_b) and precipitation observations in this study. (a) Identification of cold cloud system (CCS) based on T_b signatures, (b) tracking of CCS between two consecutive times, (c) linking all consecutive times to produce tracks, (d) matches tracked CCS with associated precipitation feature (PF), and (e) identification of MCS based on PF characteristics. The yellow shading in (e) denotes the mesoscale period as defined by CCS > 40,000 km², with a PF major axis length larger than 100 km for longer than four continuous hours. During this period, the PF area, mean rain rate, and rain rate skewness must exceed the thresholds denoted by the magenta dash lines, and the heavy rain volume ratio during this period must be larger than X% (a function of lifetime, see Figure 3) to qualify as an MCS. See text for more details. MCS, Mesoscale convective system.
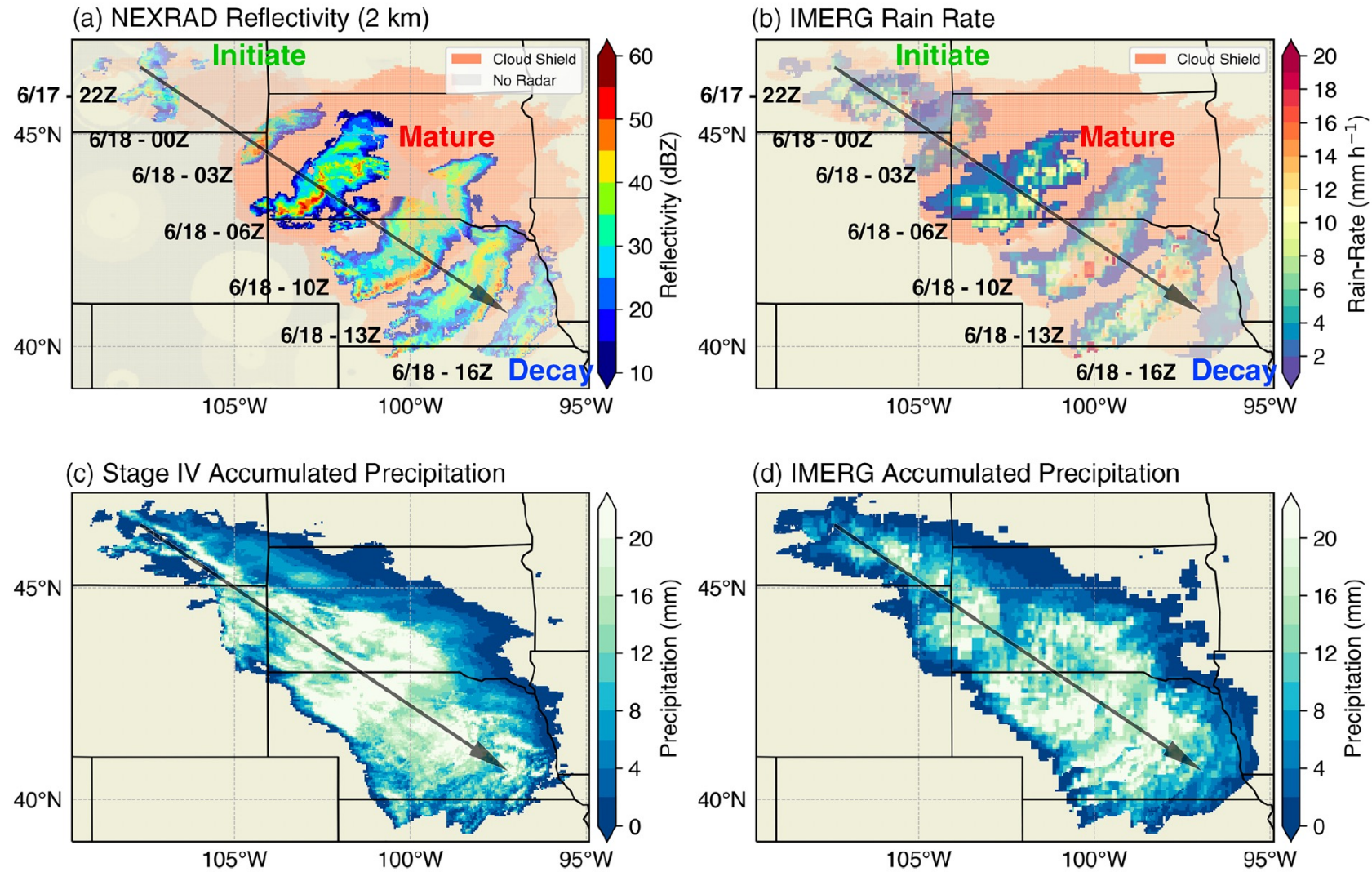
Figure 2. Example of a tracked MCS over the US Great Plains depicted by NEXRAD radar network and GPM IMERG observations. (a) Snapshots of NEXRAD radar reflectivity at 2-km MSL during various MCS lifecycle stages, (b) similar to (a) except for IMERG instantaneous rain rate, (c) Stage IV accumulated precipitation for the tracked MCS, and (d) same as (c) except for IMERG accumulated precipitation. GPM, Global Precipitation Measurement; IMERG, Integrated Multi-satellitE Retrievals for GPM; MCS, mesoscale convective system.
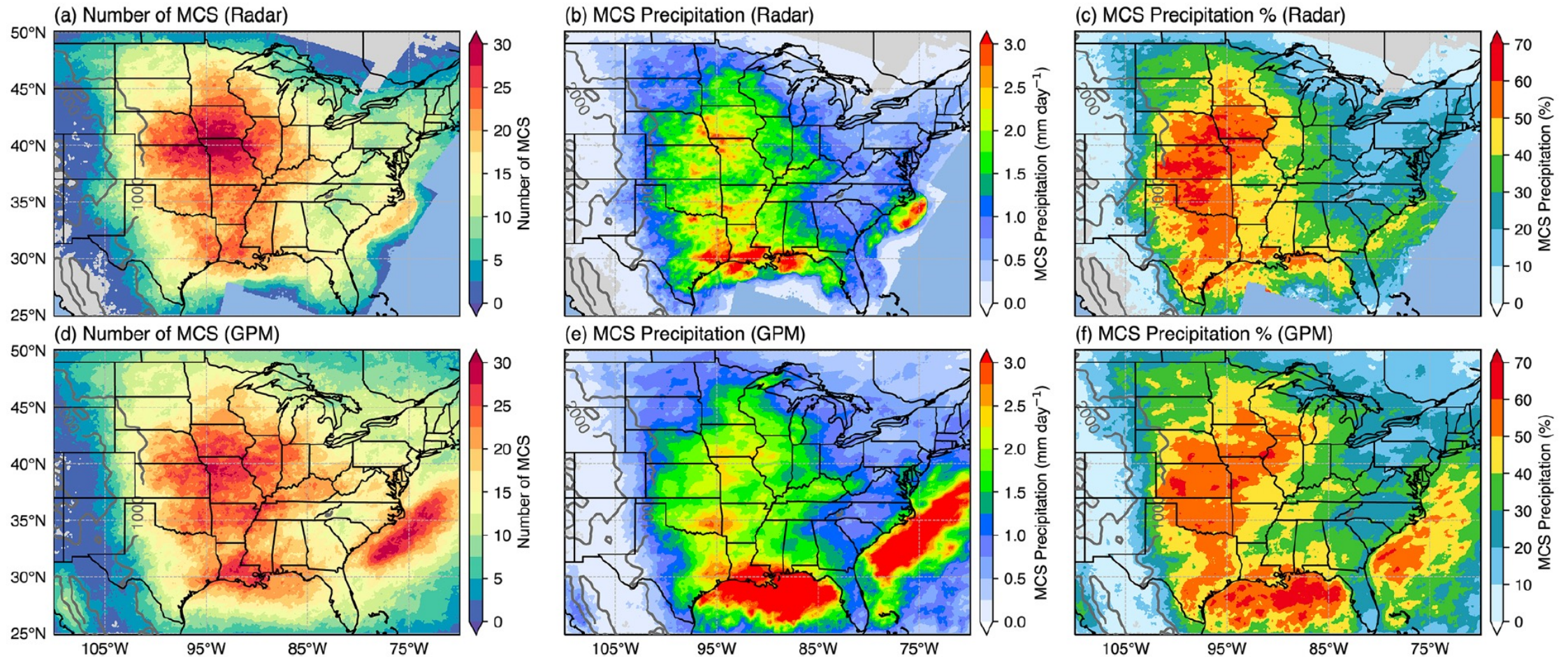
Figure 4. Comparison of the spatial distribution of observed warm season (March–August) MCSs tracked by NEXRAD radar data set (top row) and GPM IMERG data set (bottom row) for 2014–2016. (a, d) Number of MCSs, (b, e) MCS precipitation amount, and (c, f) MCS precipitation percentage to total precipitation. The number of MCSs in (a, d) is calculated by adding each swath of an MCS PF during its lifetime (counted as one sample over each grid point within the swath) over three warm seasons divided by the total number of seasons (3). GPM, Global Precipitation Measurement; IMERG, Integrated Multi-satellitE Retrievals for GPM; MCS, mesoscale convective system.
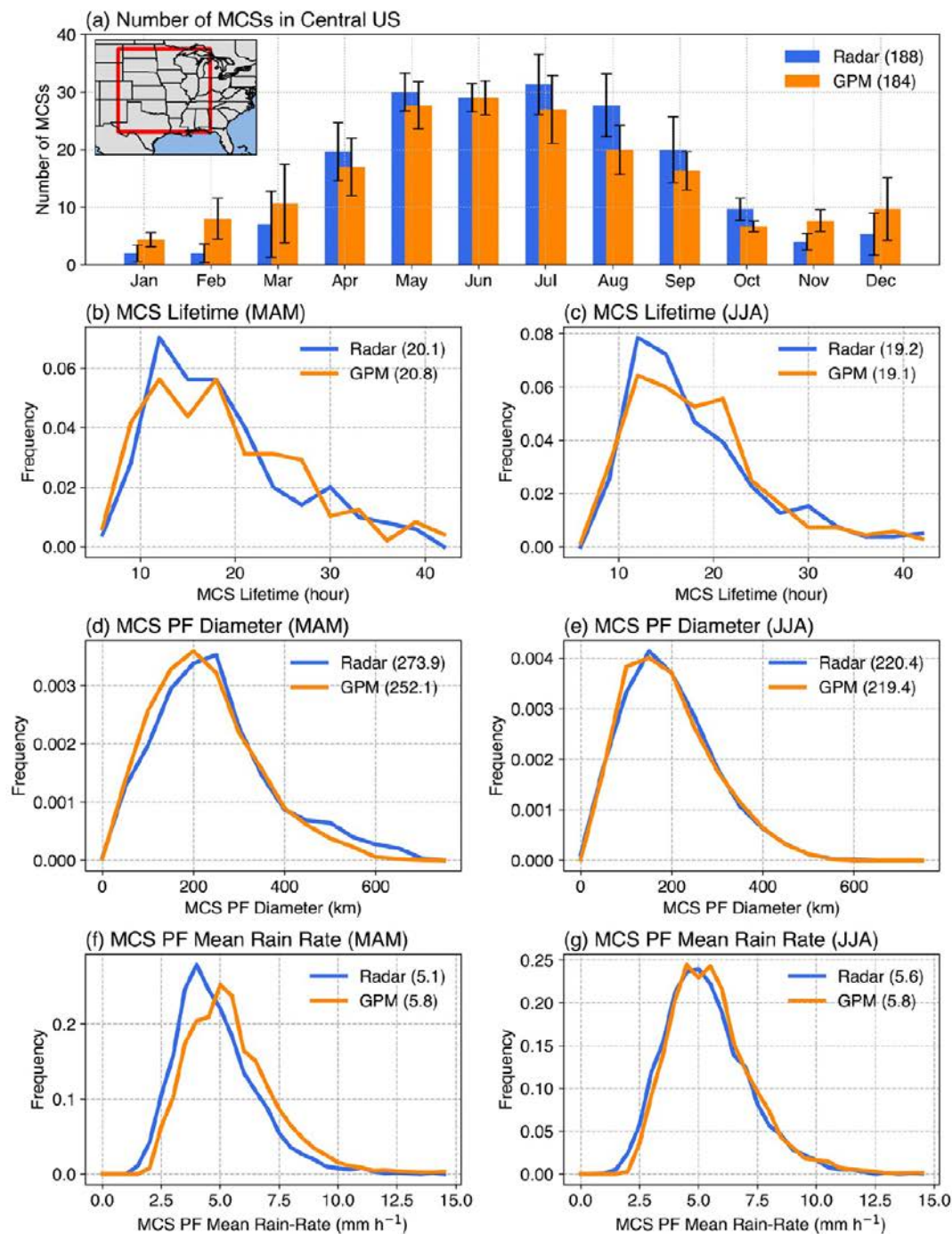
Figure 5. Comparison of MCS statistics over Central United States tracked by NEXRAD radar data set and GPM IMERG data set during 2014–2016. (a) Monthly average number of MCS (bars) and standard deviation (error bars), probability density function (PDF) of MCS properties are shown in (b–g) for MAM (left column), and JJA (right column), respectively. (b, c) MCS lifetime, (d, e) MCS PF diameter, (f, g) MCS PF mean rain rate. The region of comparison is shown as the red box in the inset of (a). GPM, Global Precipitation Measurement; IMERG, Integrated Multi-satellitE Retrievals for GPM; MCS, mesoscale convective system; PF, precipitation feature.

Figure 6. Comparisons of MCSs over northeastern China tracked by using ground-based radar network data and GPM IMERG data during 2016. (a) Distribution of MCS lifetime, and (b) number of MCSs per month. The region of comparison is shown as the red box in the inset of (b). GPM, Global Precipitation Measurement; IMERG, Integrated Multi-satellitE Retrievals for GPM; MCS, mesoscale convective system.

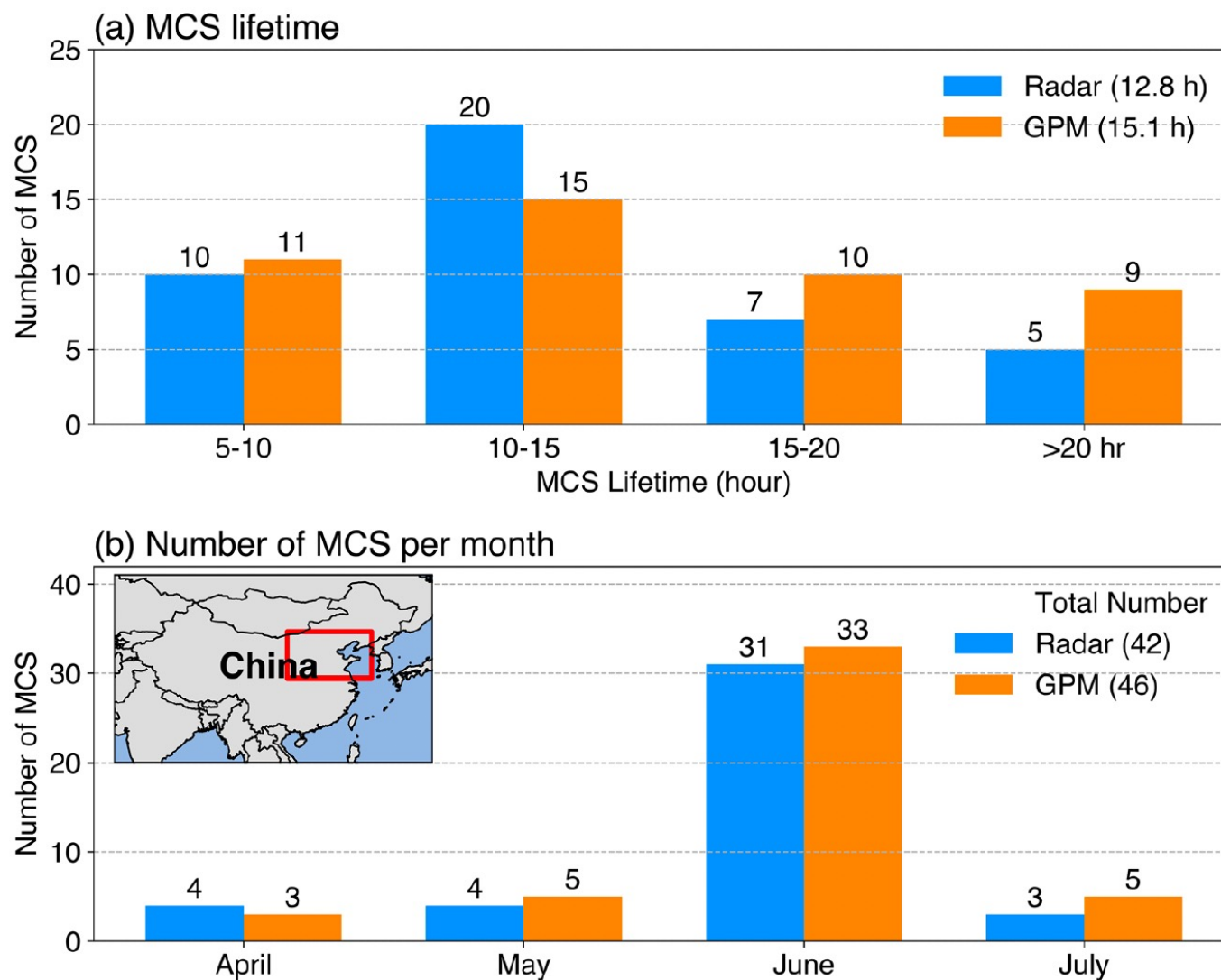**Figure 7.** Example snapshot of tracked MCSs over the Maritime Continent at 10:30 UTC on January 21, 2019. (a) Infrared brightness temperature, (b) GPM IMERG precipitation. The magenta contours in (a) and the color shadings behind large clusters of PFs in (b) denote each tracked MCS. Weak rain rates <2 mm h^{-1} in (b) are excluded for clarity. Animation for this day is provided in the Supporting Information. GPM, Global Precipitation Measurement; IMERG, Integrated Multi-satellitE Retrievals for GPM; MCS, mesoscale convective system; PF, precipitation feature.
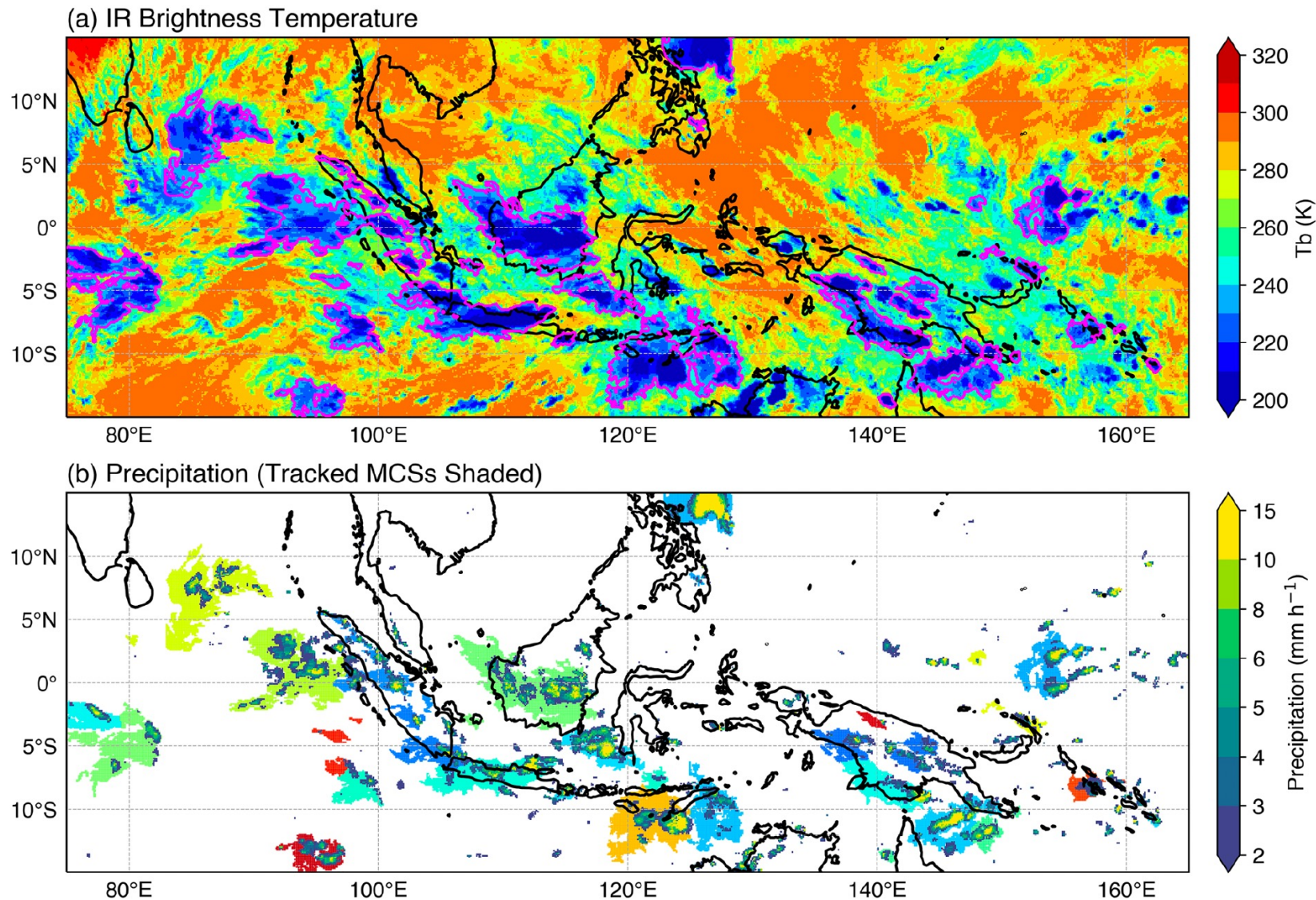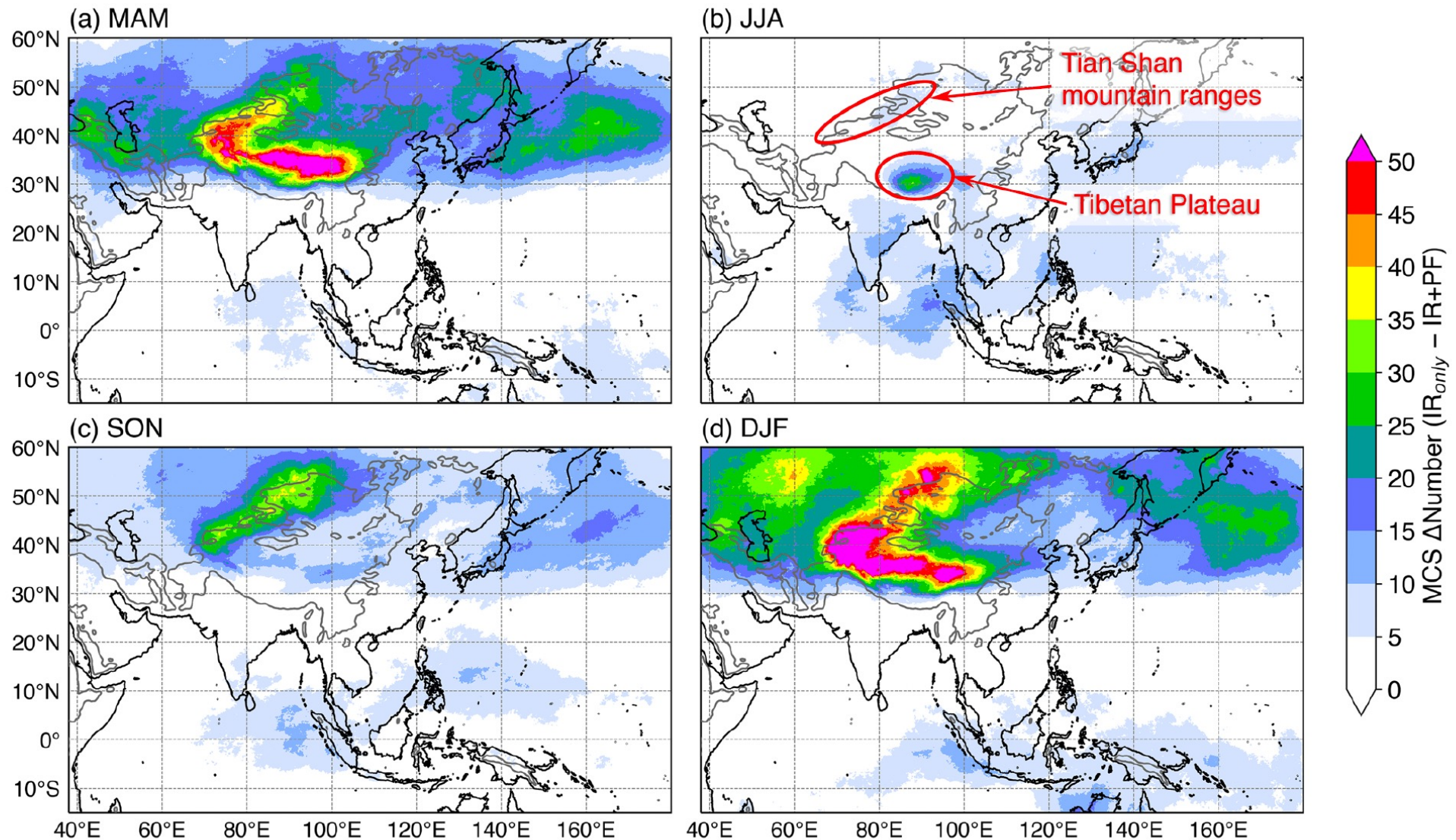
Figure 8. Spatial distribution of the average differences in the number of MCSs between the IR-only method and the new robust MCS method in this study during the four seasons for 2014–2019. (a) March–May, (b) June–August, (c) September–November, and (d) December–February. Gray outlines in the background are terrain elevations higher than 1,000 m. MCS, mesoscale convective system.
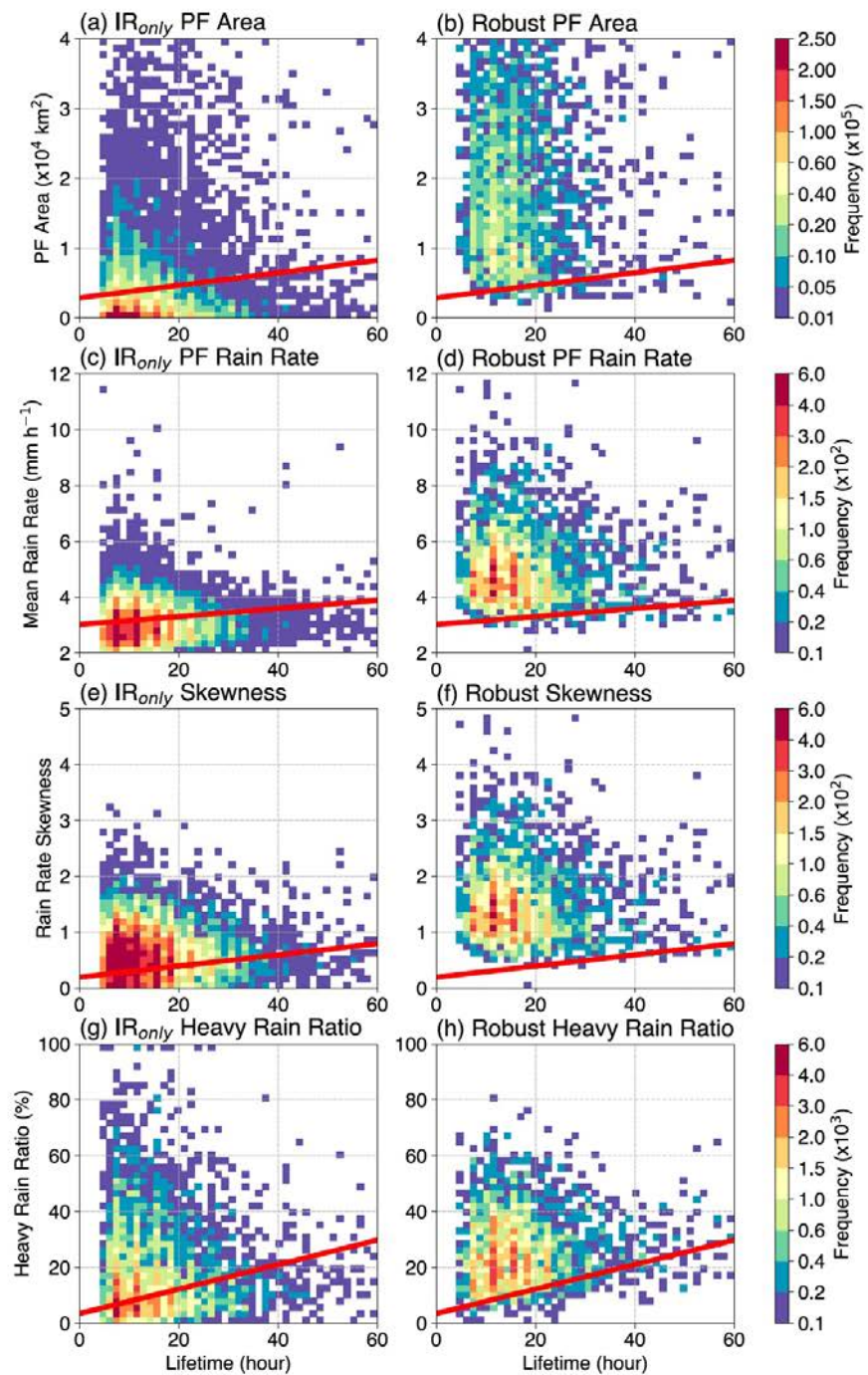
Figure 9. Comparisons of the joint PDF of PF parameters between MCSs defined by the IR-only method (left column) and the new IR + PF method (right column) over Central Asia region (28°N–60°N, 50°E–120°E) for all seasons during 2014–2019. (a, b) PF area, (c, d) PF mean rain rate, (e, f), PF rain rate skewness, and (g, h) heavy rain ratio. Red lines denote thresholds used to define robust MCSs for each PF parameter. The MCS lifetime here is defined by the tracked CCS duration. Mean values of the PF parameters throughout each MCS lifetime are used. IR, infrared; MCS, mesoscale convective system; PDF, probability density function; PF, precipitation feature.
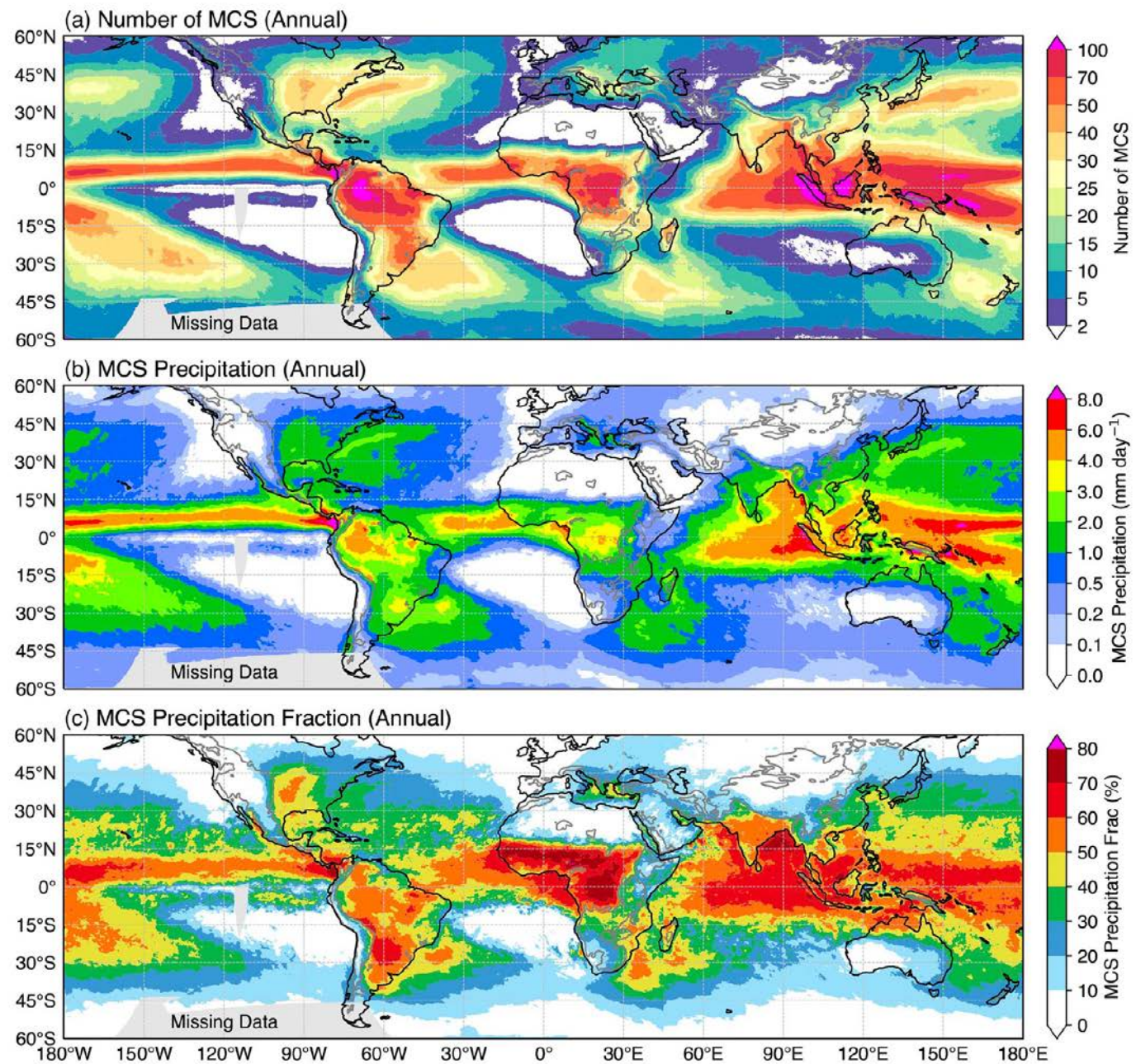
Figure 10. Annual mean global distribution of (a) the number of MCS, (b) MCS precipitation amount, and (c) percentage of MCS precipitation to total precipitation between 2001 and 2019. Dark gray contours show terrains higher than 1,000 m. The gray shaded regions over the Southern Pacific Ocean have frequent (>25%) missing T_b data that affects MCS tracking and is therefore masked out. MCS, mesoscale convective system.
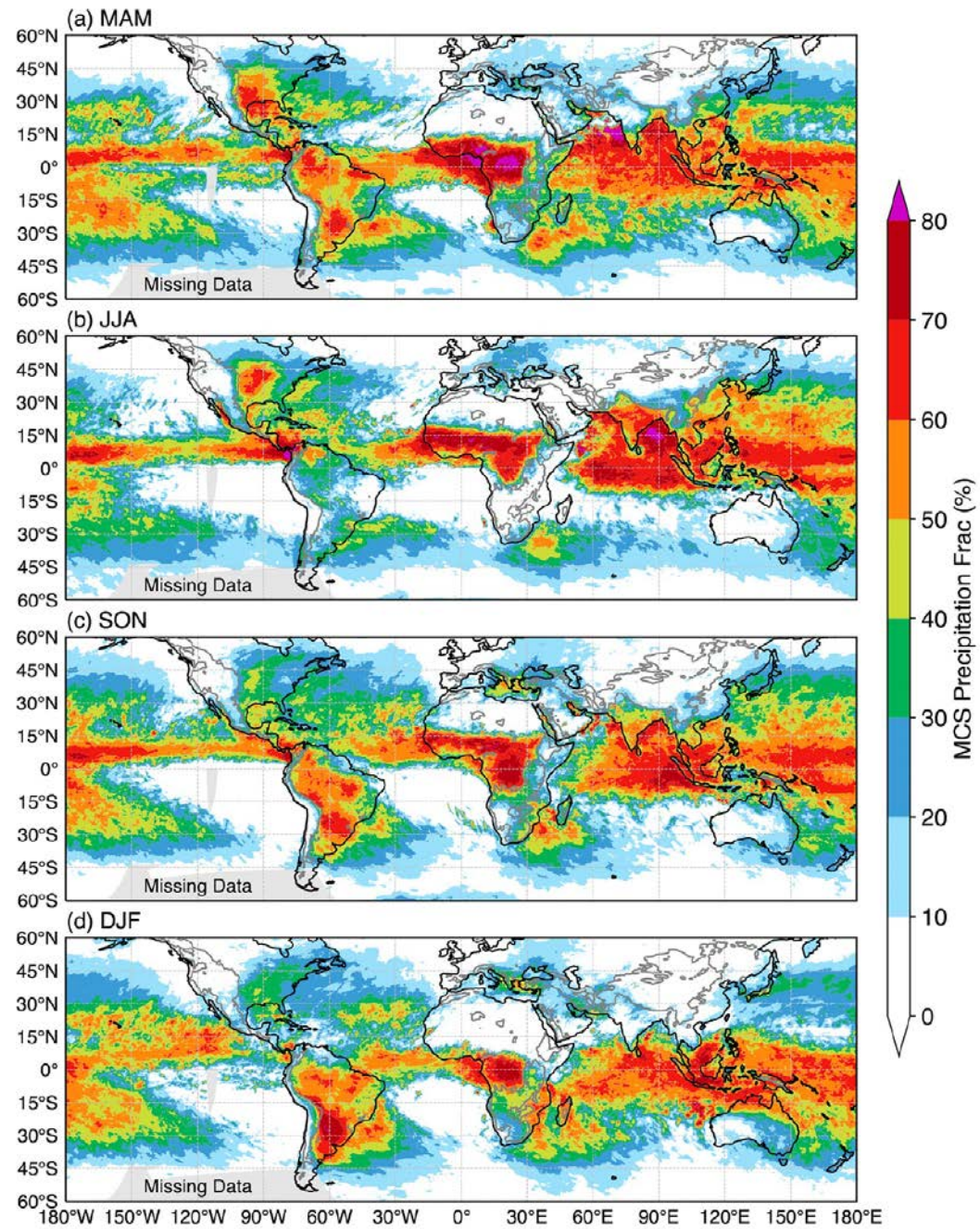
Figure 11. Percentage of MCS precipitation to total precipitation in (a) March–May, (b) June–August, (c) September–November, and (d) December–February. MCS, mesoscale convective system.
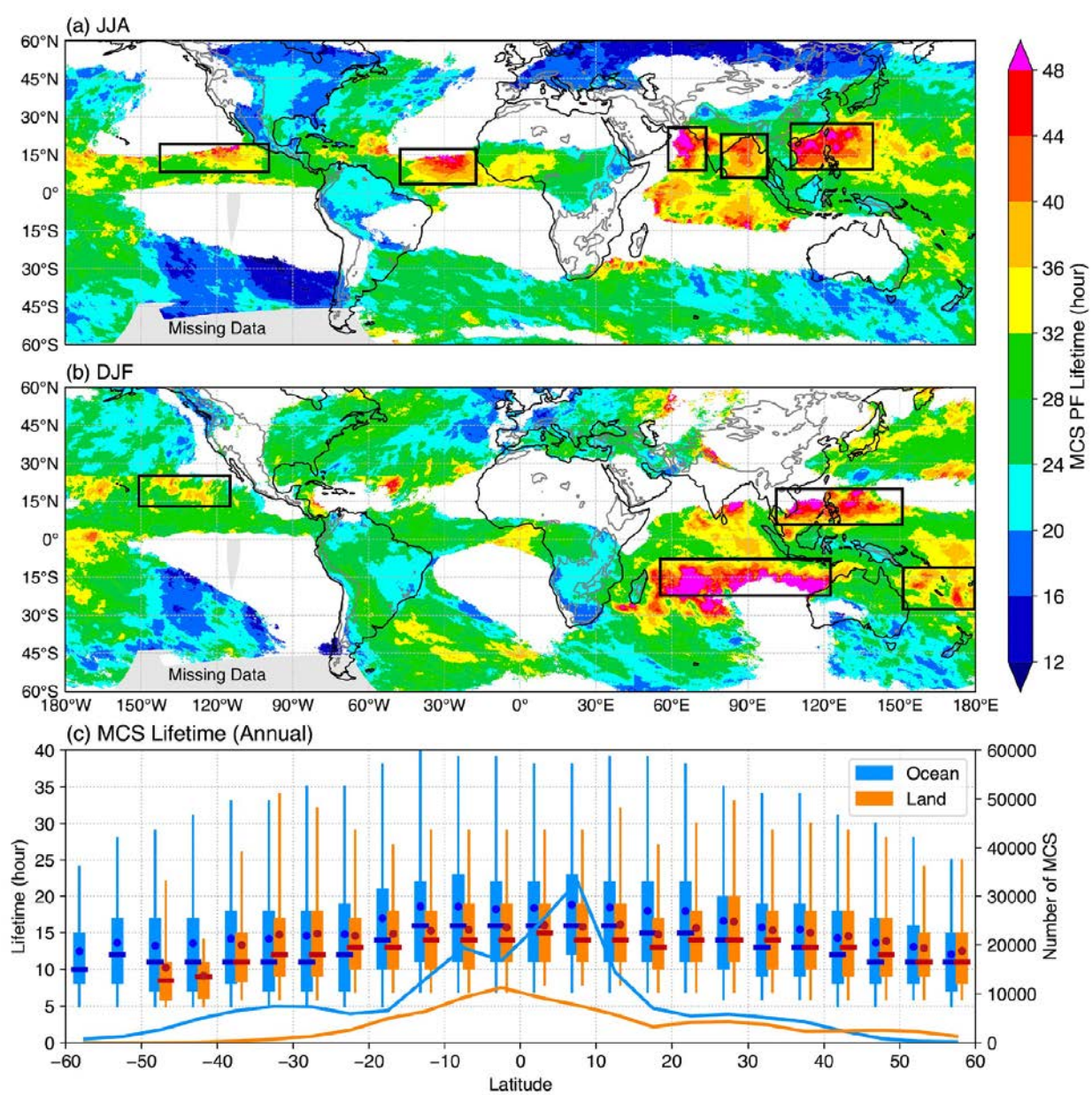
Figure 12. Spatial distribution of mean MCS lifetime during (a) JJA and (b) DJF, (c) box-whisker plot of the zonal MCS lifetime distribution for oceanic and land MCSs. Areas with average number of MCS <1 are excluded in (a, b). To calculate the spatial distribution, each MCS PF (rain rate >2 mm h^{-1}) swath during its entire lifetime is assigned a single lifetime value (in hours) on the native 0.1° pixel, and then averaged over time in a season. Regions with long-lived MCS are marked in black boxes, see discussions in the text. In (c), boxes are the interquartile range, horizontal bars are median values, circles are mean values, and whiskers denote 5th and 95th percentile values. The two thick lines in (c) are the number of MCS per latitude bin. MCS, mesoscale convective system; PF, precipitation feature.
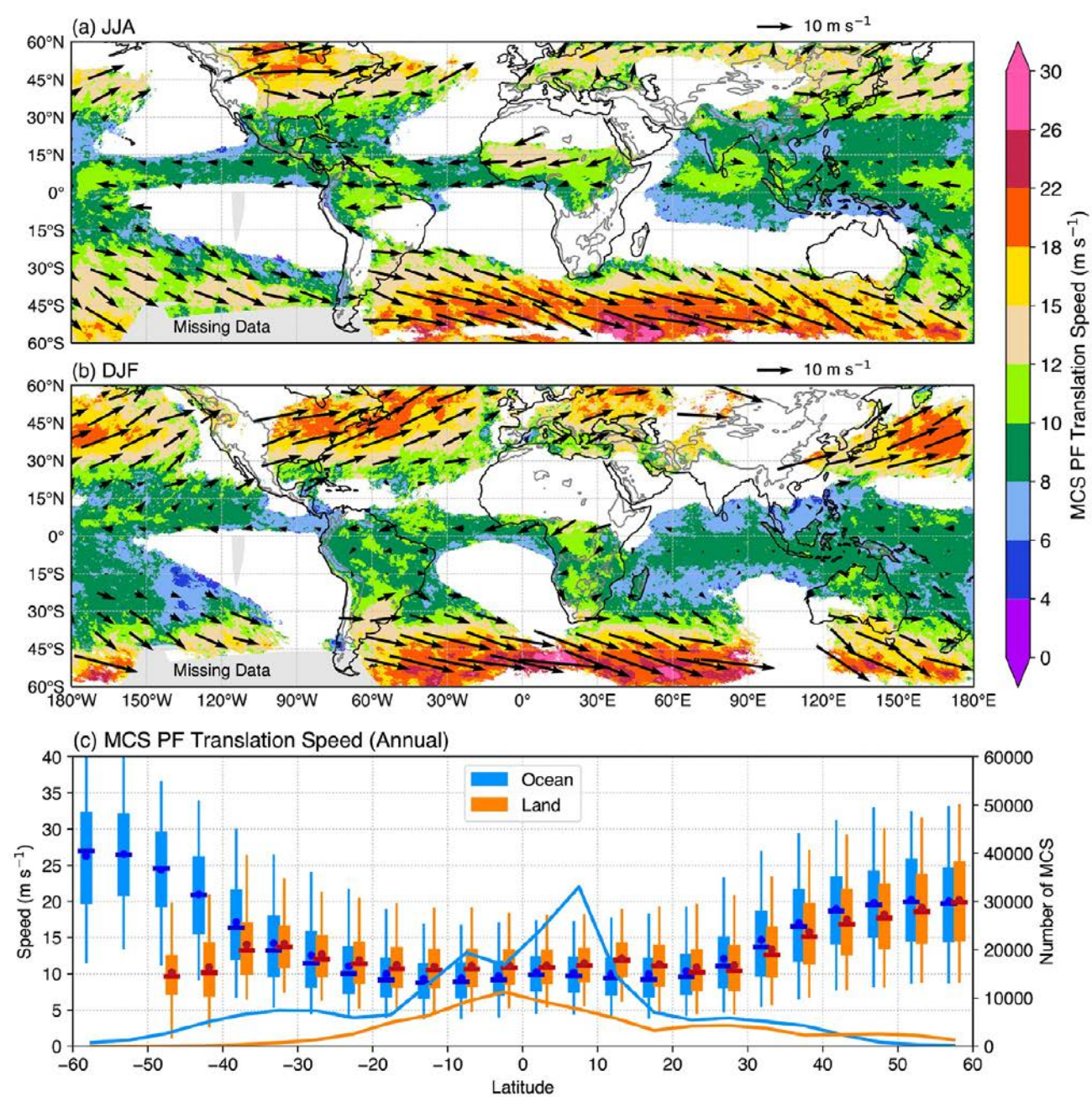
Figure 13. Same as Figure 12 except for MCS translation speeds and directions. The shadings denote mean translation speed, the vectors show the translation direction and magnitude, which are estimated by using a 2D cross-correlation map between two consecutive hours of the MCS precipitation features (Feng et al. 2018). MCS, mesoscale convective system.
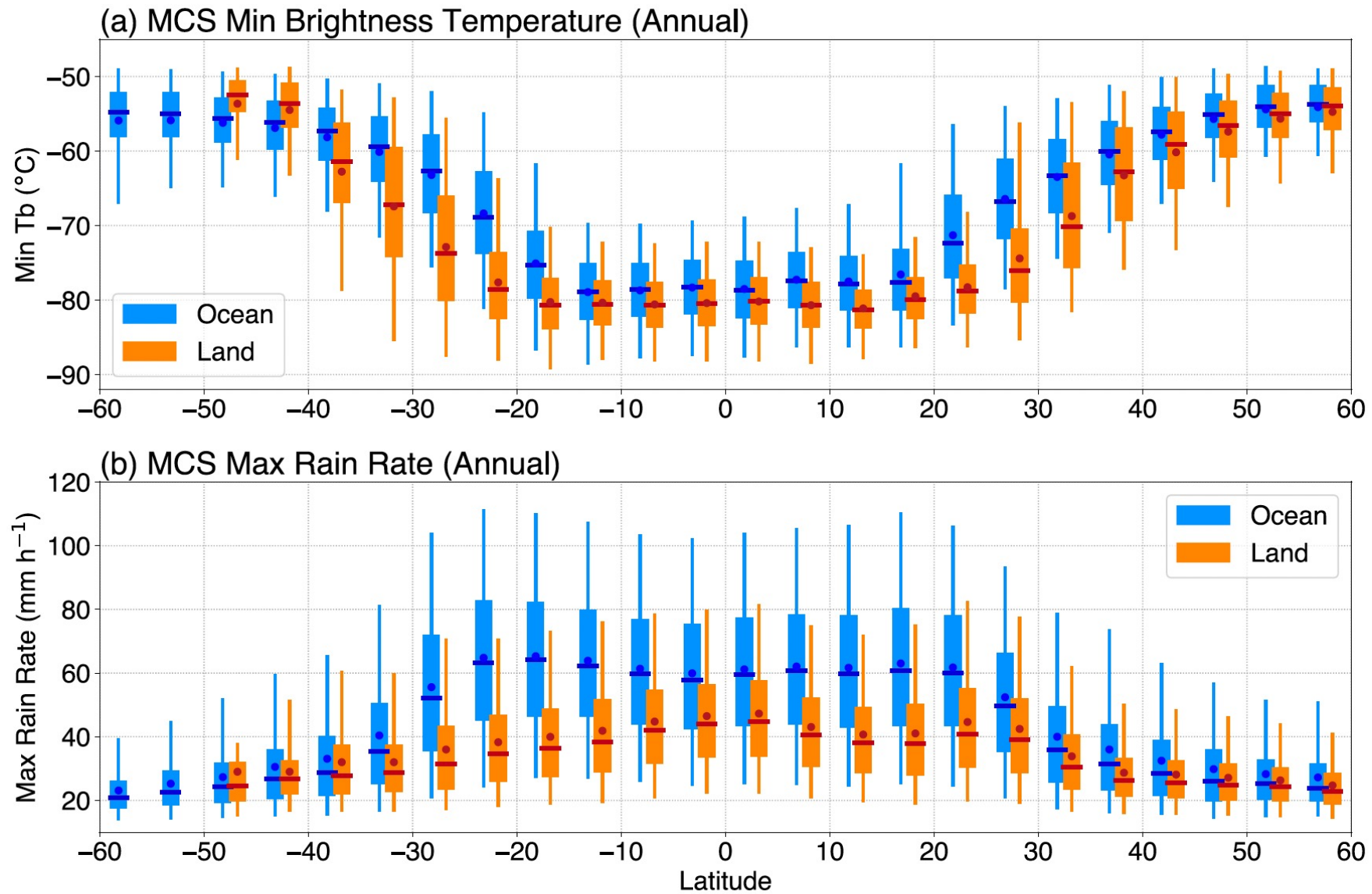
Figure 14. Box-whisker plot of the zonal distribution of (a) minimum IR T_b for each MCS, and (b) maximum rain rate for each MCS. Boxes are the interquartile range, horizontal bars are median values, circles are mean values, and whiskers denote 5th and 95th percentile values. MCS, mesoscale convective system.

ARTICLE

More frequent intense and long-lived storms dominate the springtime trend in central US rainfall

Zhe Feng[1], L. Ruby Leung[1], Samson Hagos[1], Robert A. Houze[1], Casey D. Burleyson[1] & Karthik Balaguru[1]

MCS mean rainfall and trend (April–June 1979–2014)
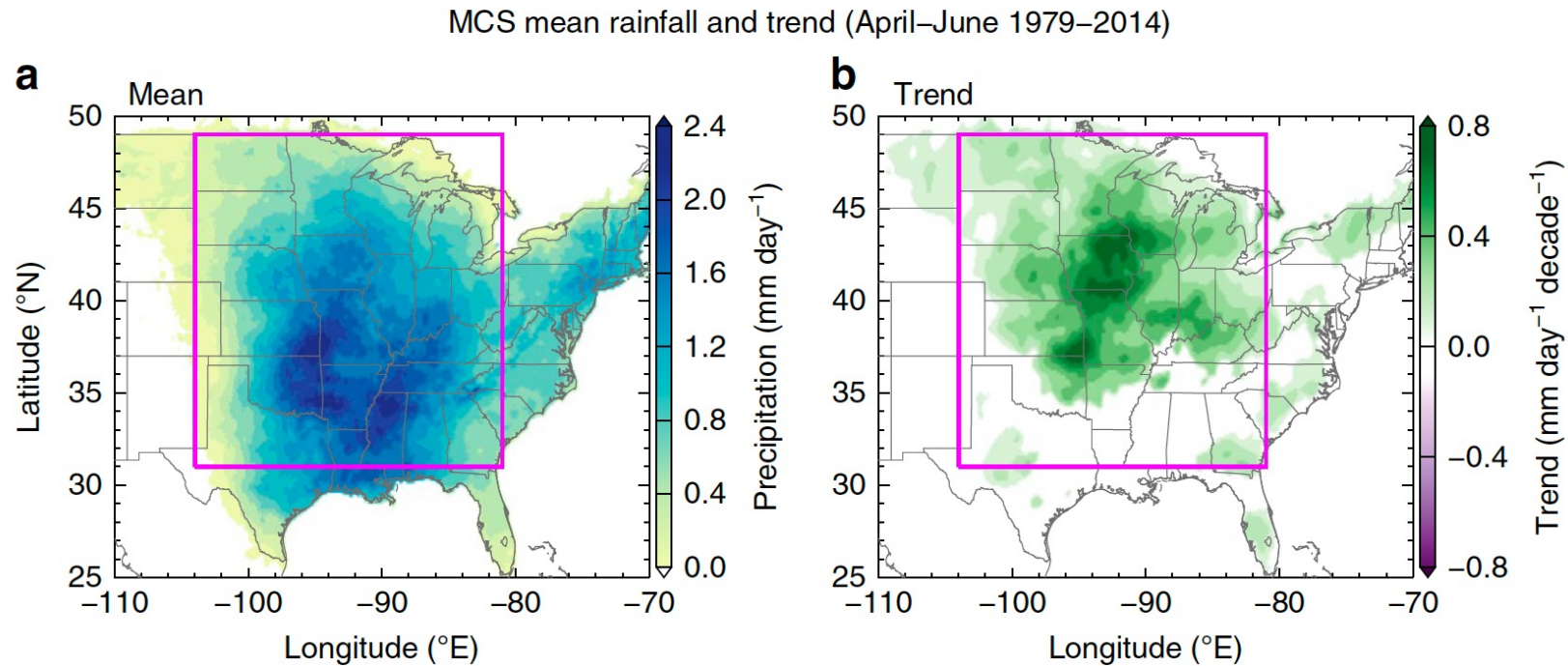
Figure 1 | Springtime mesoscale convective systems rainfall climatology and trends. Mesoscale convective system (MCS) (**a**) mean total rainfall and (**b**) total rainfall trend from 1979 to 2014. Total rainfall shown is the accumulated MCS rainfall during April–June divided by the total number of days (91). Only trends with statistical significance above 95% using a two-tailed Student t-test are shown. Data within the magenta boxes are used to calculate the trends in Fig. 2.

a Total precipitation

1979–2014 (3% decade^{-1})*
1997–2014 (4% decade^{-1})++

b MCS precipitation

1979–2014 (25% decade^{-1})
1997–2014 (28% decade^{-1})

c Non–MCS precipitation

1979–2014 (−2% decade^{-1})*
1997–2014 (−23% decade^{-1})

d MCS lifetime

1979–2014 (4% decade^{-1})
1997–2014 (5% decade^{-1})

e MCS precipitation frequency

1979–2014 (11% decade^{-1})
1997–2014 (26% decade^{-1})

f Non–MCS precipitation frequency

1979–2014 (−8% decade^{-1})
1997–2014 (−14% decade^{-1})

Figure 2 | Time series and linear trends of precipitation in the Central United States. Linear trends of April–June (**a**) total precipitation, (**b**) mesoscale convective system (MCS) precipitation, (**c**) non-MCS precipitation, (**d**) MCS lifetime, (**e**) MCS precipitation frequency and (**f**) non-MCS precipitation frequency. Precipitation frequency is calculated on the NASA North American Land Data Assimilation System (NLDAS) native grid-scale by dividing the number of hours of MCS or non-MCS precipitation (hours with rain-rate >1 mm h^{-1}) by the total number of hours in each season. Results are calculated within the area of the magenta boxes in Fig. 1. Green boxes show the area between the 25th and 75th percentiles, whiskers denote the 5th and 95th percentiles. Mean values are the black lines with solid circles while regression fit lines to the mean values are the magenta (1979–2014 period) and blue (1997–2014 period) lines. The time period before incorporation of the national radar network data in NLDAS is shaded in gray. Linear trends normalized by the 36-year mean are provided for the entire period (1979–2014) and for the radar period (1997–2014) in the legend of each panel. All trends are statistically significant at 95% confidence interval with a two-tailed Student *t*-test, except those marked with *which are only significant at 90%. Those marked with + + are not significant at 90%. The significance symbols are shown in the legend of each panel.
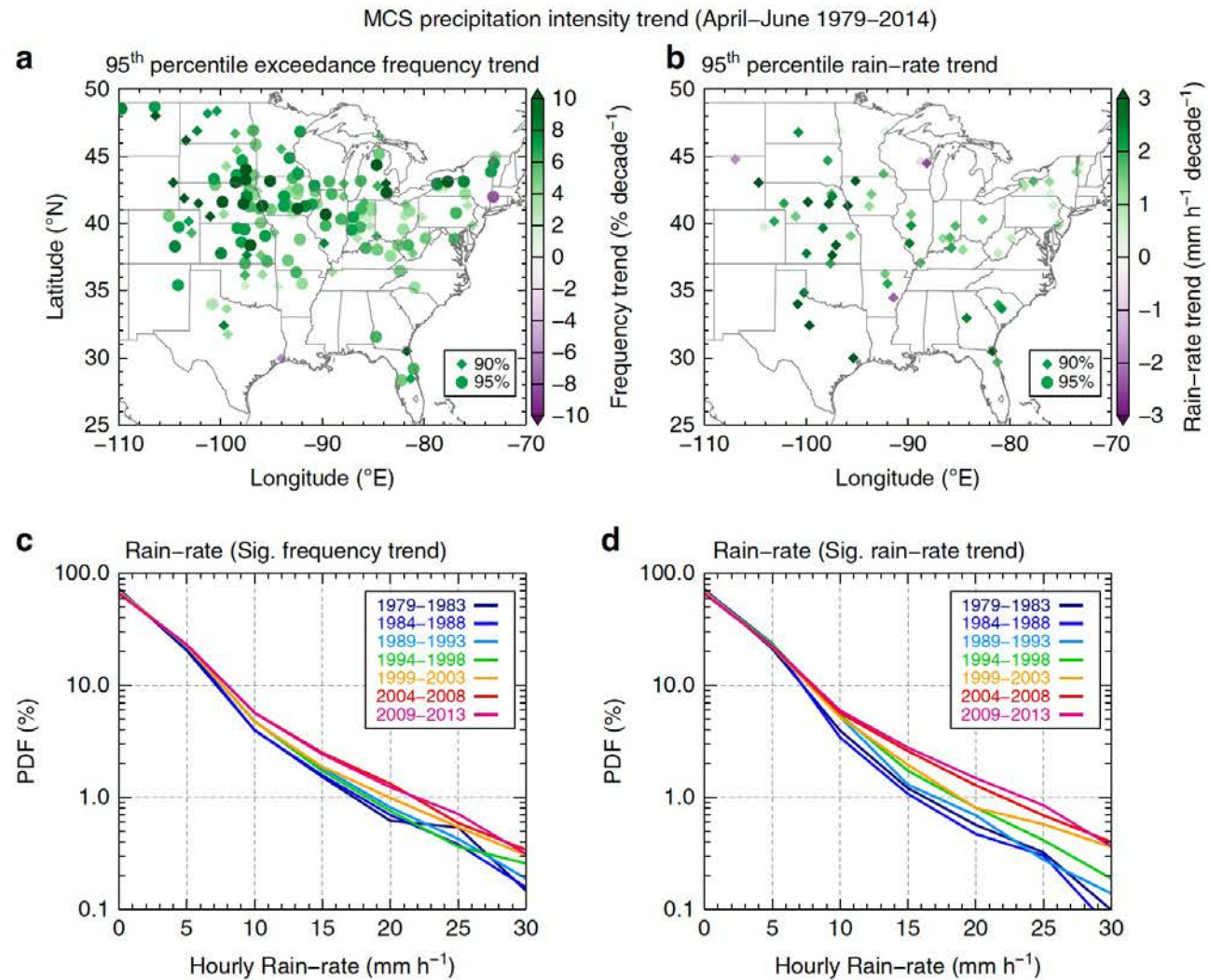
Figure 3 | Mesoscale convective system extreme precipitation intensity trends. Trends in mesoscale convective system (MCS) (**a**) exceedance frequency of the 95th percentile hourly rain-rate, (**b**) the actual 95th percentile hourly rain-rate, (**c**) probability density function (PDF) of hourly rain-rates from stations with a significant (Sig.) exceedance frequency trend, and (**d**) PDF of hourly rain-rates from stations with a significant rain-rate trend. The trends are obtained using individual hourly rain gauge data (see the text for more details). Circle and diamond symbols in **a** and **b** show trends that are statistically significant at 95% and 90% with a two-tailed Student t-test, respectively. PDFs in **c** and **d** are constructed using data from all stations with 90% statistically significant trends.
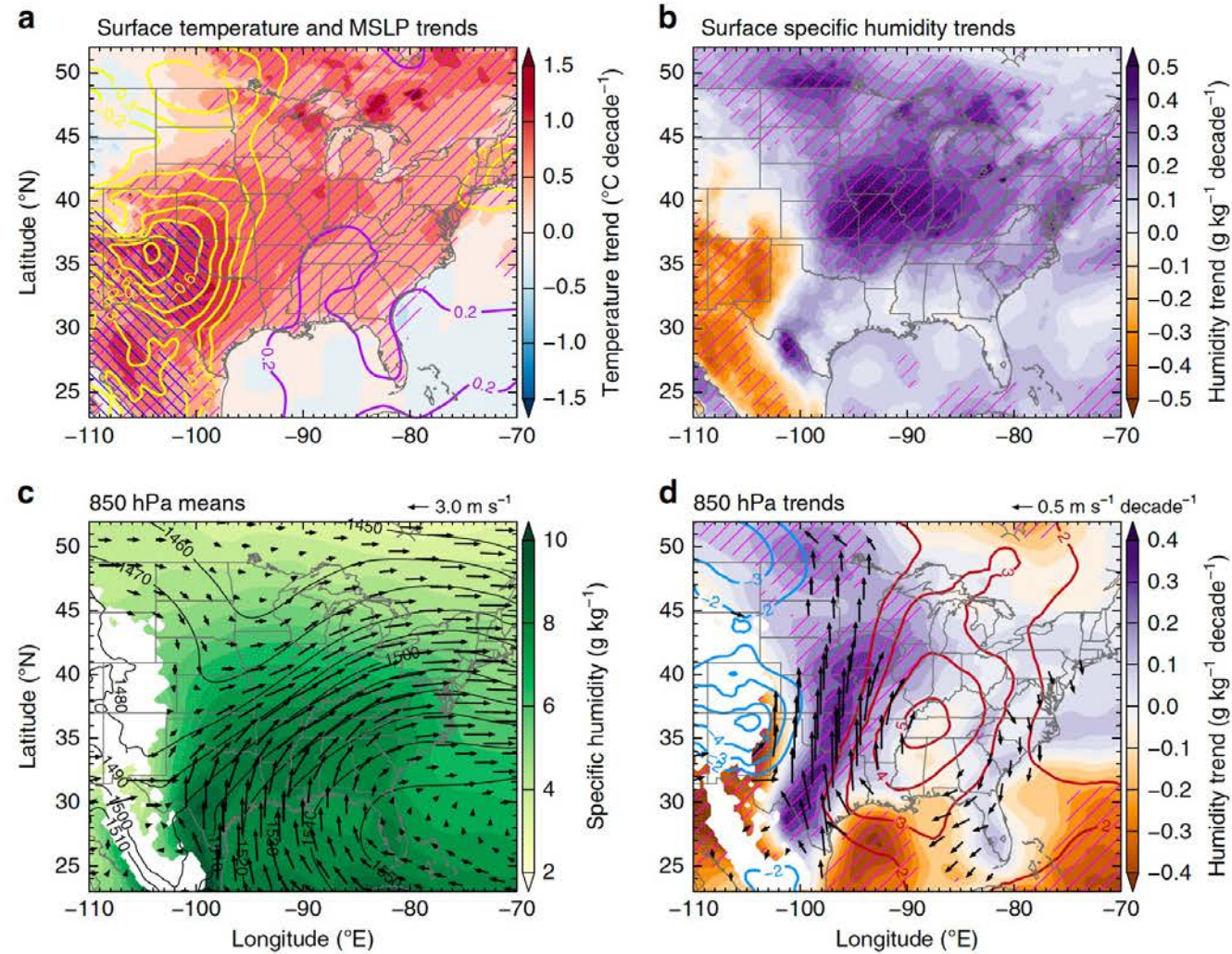
Figure 4 | Large-scale environment climatology and trends during occurrence of high-precipitation mesoscale convective systems. (**a**) Surface temperature (shaded) and mean sea level pressure (MSLP) trends (MSLP contours in 0.1 hPa per decade intervals, purple/yellow contours denote positive/ negative MSLP trends), (**b**) surface specific humidity trends (shaded), (**c**) 850 hPa mean specific humidity (shaded), geopotential height (contours, in 10 m intervals), and wind (arrows), and (**d**) 850 hPa trends in specific humidity (shaded), geopotential height (contours, in 1 m per decade intervals, red/blue contours denote positive/negative geopotential height trends), and wind (arrows, statistically significant at 95%). Grid points with a statistical significance exceeding the 95% confidence interval are marked by (**a**) pink hashes for temperature and blue hashes for MSLP, (**b,d**) purple hashes for specific humidity. Areas with mean surface pressure below 850 hPa are masked out in **c** and **d**.

LETTER
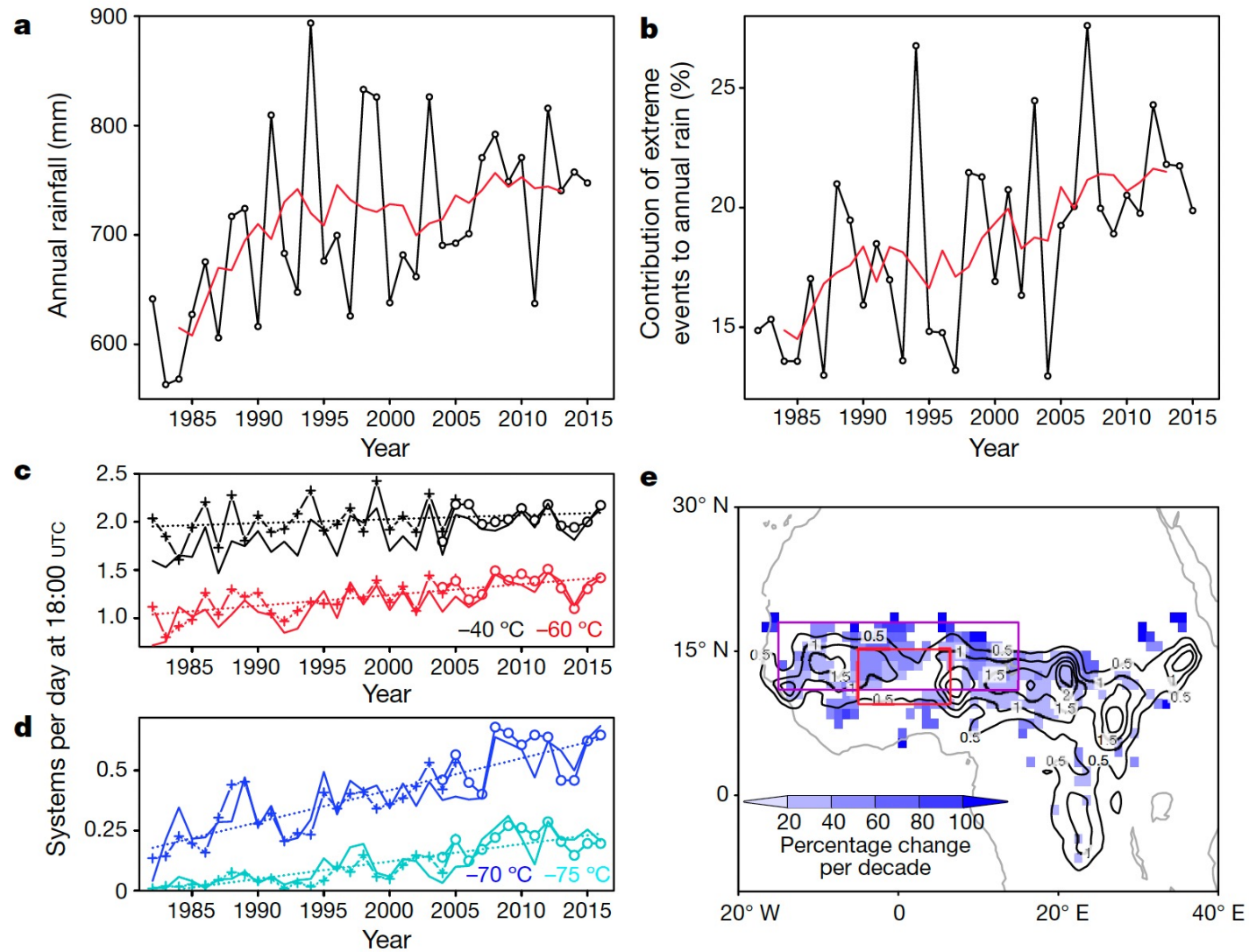
Frequency of extreme Sahelian storms tripled since 1982 in satellite observations

Christopher M. Taylor[1,2], Danijel Belušić[1,3], Françoise Guichard[4], Douglas J. Parker[5], Théo Vischel[6], Olivier Bock[7], Phil P. Harris[1,2], Serge Janicot[8], Cornelia Klein[1] & Gérémy Panthou[6]

Figure 1 | Trends in MCS and rainfall characteristics across the Sahel. a, b, Annual rainfall (**a**), and contribution of extreme events to annual rainfall (**b**), as measured by a daily rain-gauge network. Red lines indicate five-year running means. **c, d,** Regional MCS frequency at 1800 UTC at different temperature thresholds, derived directly from measurements onboard the Meteosat First Generation (MFG; + symbols) and Meteosat Second Generation (MSG; O symbols) geostationary satellites. The cross-calibrated GridSat version of these data is shown as a solid line. Dotted lines denote trends. **e,** Significant trends ($P < 0.05$) in MCS cloud cover at 1800 UTC (using a temperature threshold of −70 °C). Trends are expressed as a percentage change per decade, relative to the 35-year mean (contours). The red and purple rectangles denote the domains used in **a, b** and **c, d,** respectively.

Table 1 | Linear correlation statistics for 24-hour mean MCS frequencies at different temperature thresholds

| Temperature threshold (°C)	Correlation coefficient (P value)		
	Linear trend	Sahel rain	Global temperature
−40	0.41 (0.007)	0.88 (<0.00001)	0.37 (0.0162)
−60	0.77 (<0.00001)	0.83 (0.00015)	0.77 (<0.00001)
−70	0.87 (<0.00001)	0.65 (0.00002)	0.82 (<0.00001)
−75	0.88 (<0.00001)	0.56 (0.00036)	0.80 (<0.00001)

Global land mean temperatures (shown in Extended Fig. 1c) are computed from JJAS averages.
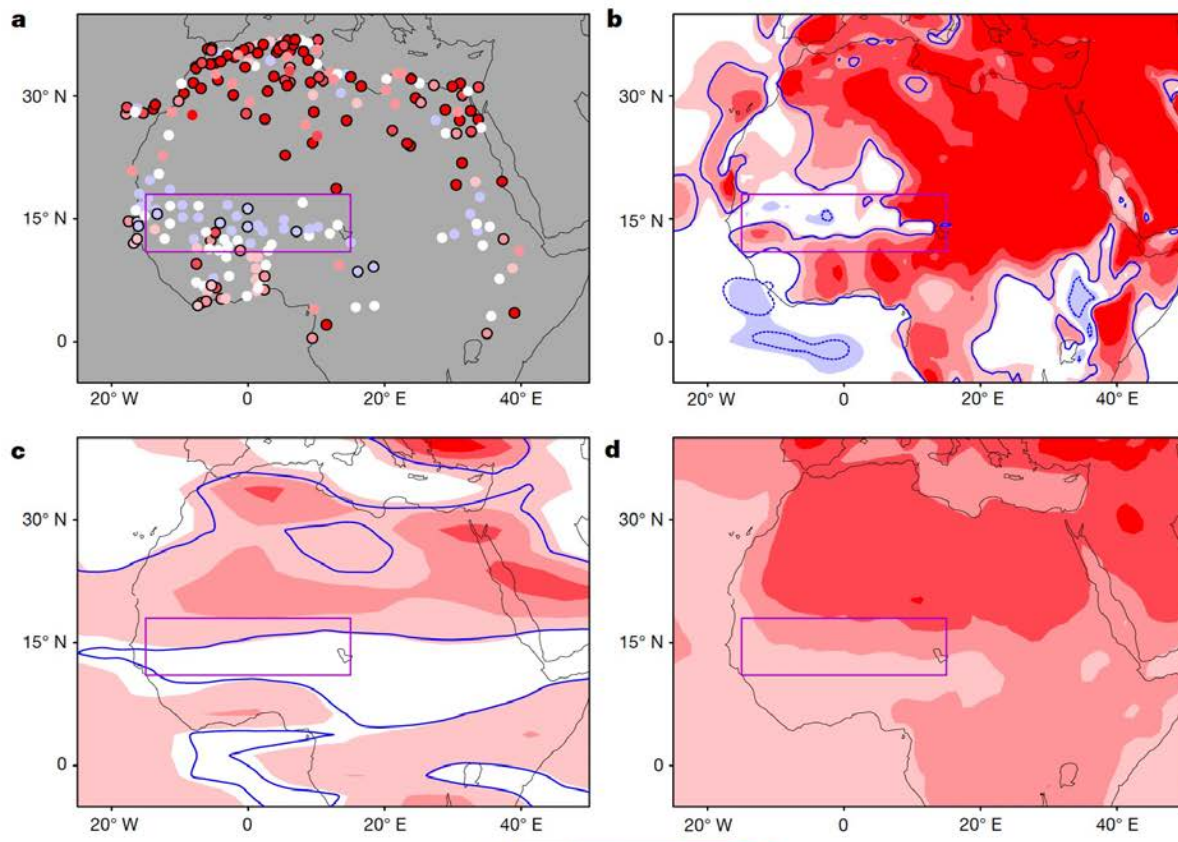
Figure 2 | Temperature trends (for June to September) in observations and models. a–d, Trends (shown as change in temperature (°C) per decade) are derived from: **a**, synoptic stations; **b**, ERA-Interim reanalysis; **c**, lower tropospheric temperature derived from microwave sounding data; and **d**, CMIP5-ensemble-based mean for historical runs. **e**, The meridional temperature gradient (20° N minus 10° N; average over 15° W to 15° E) from the CMIP5 historical (red), RCP4.5 (green) and RCP8.5 (purple) ensembles (relative to 1961–1990; shading denotes the standard deviation for each ensemble). Temperatures were taken at a height of 2 metres, except in panel **c**, which samples the lower troposphere. Trends are computed for the period 1982–2015, except in panel **d**, which covers 1976–2005. Significant positive and negative trends ($P < 0.05$) are denoted by solid black circles (**a**), or lie within blue contours (**b**, **c**). The rectangles mark the region of the Sahel that was used for computing MCS statistics.
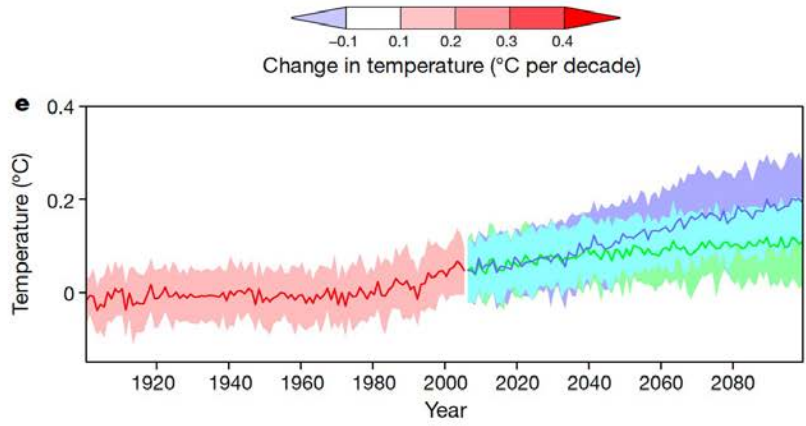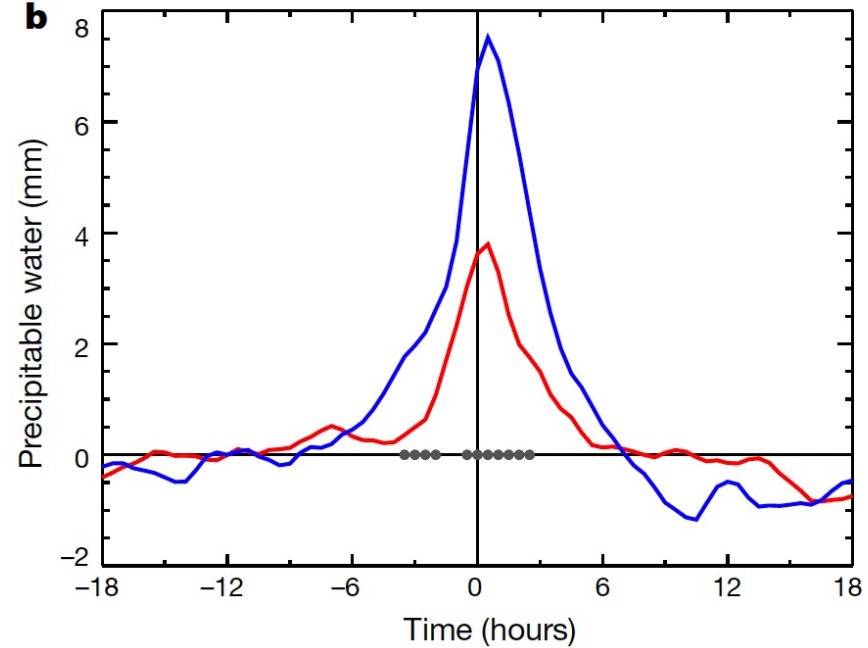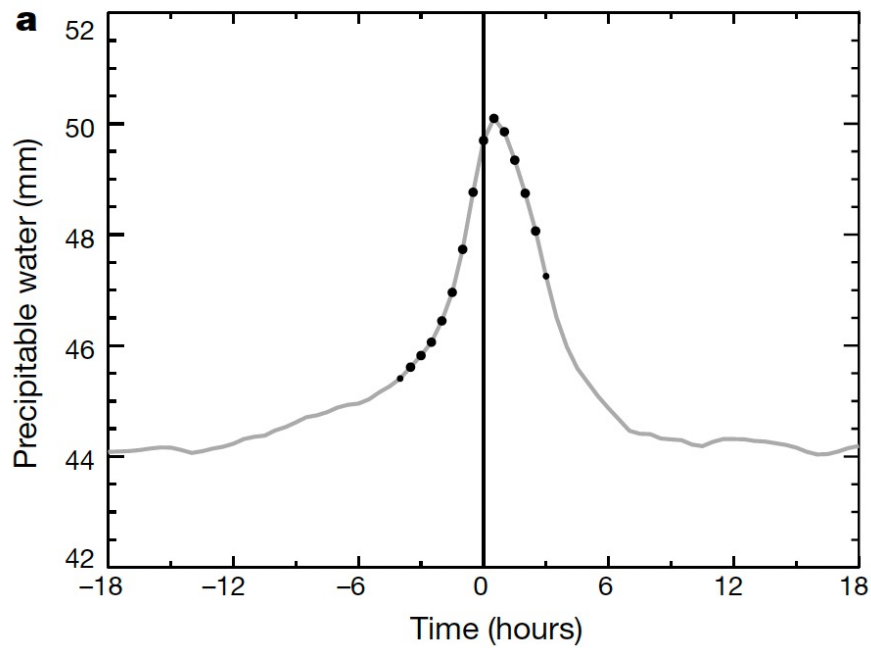
Figure 3 | Evolution of observed precipitable water, measured at GPS stations. a, Composite mean precipitable water (mm) associated with the passage (at 0 h) of 496 Sahelian MCSs. Small (or large) circles denote times when precipitable water correlates significantly with MCS intensity at $P < 0.05$ (or $P < 0.01$). **b**, Evolution of precipitable-water anomalies sampled from events in the lower (blue) and upper (red) quartiles of MCS temperature. Circles denote times when the two time series differ significantly ($P < 0.05$).

Intensification of Mesoscale Convective Systems in the East Asian Rainband Over the Past Two Decades

Puxi Li[1] iD, **Fengfei Song**[2,3] iD, **Haoming Chen**[1], **Jian Li**[1] iD, **Andreas F. Prein**[4] iD, **Wenxia Zhang**[5] iD, **Tianjun Zhou**[5], **Moran Zhuang**[6,7], **Kalli Furtado**[8] iD, **Mark Muetzelfeldt**[9], **Reinhard Schiemann**[9] iD, and **Chao Li**[10] iD

[1]State Key Laboratory of Severe Weather, Chinese Academy of Meteorological Sciences, China Meteorological Administration, Beijing, China, [2]Frontier Science Center for Deep Ocean Multispheres and Earth System and Physical Oceanography Laboratory, Ocean University of China, Qingdao, China, [3]Laoshan Laboratory, Qingdao, China, [4]National Center for Atmospheric Research, Boulder, CO, USA, [5]LASG, Institute of Atmospheric Physics, Chinese Academy of Sciences, Beijing, China, [6]CMA Earth System Modeling and Prediction Centre, China Meteorological Administration, Beijing, China, [7]Key Laboratory of Earth System Modeling and Prediction, China Meteorological Administration, Beijing, China, [8]Met Office, Exeter, UK, [9]National Centre for Atmospheric Science, Department of Meteorology, University of Reading, Reading, UK, [10]Max Planck Institute for Meteorology, Hamburg, Germany
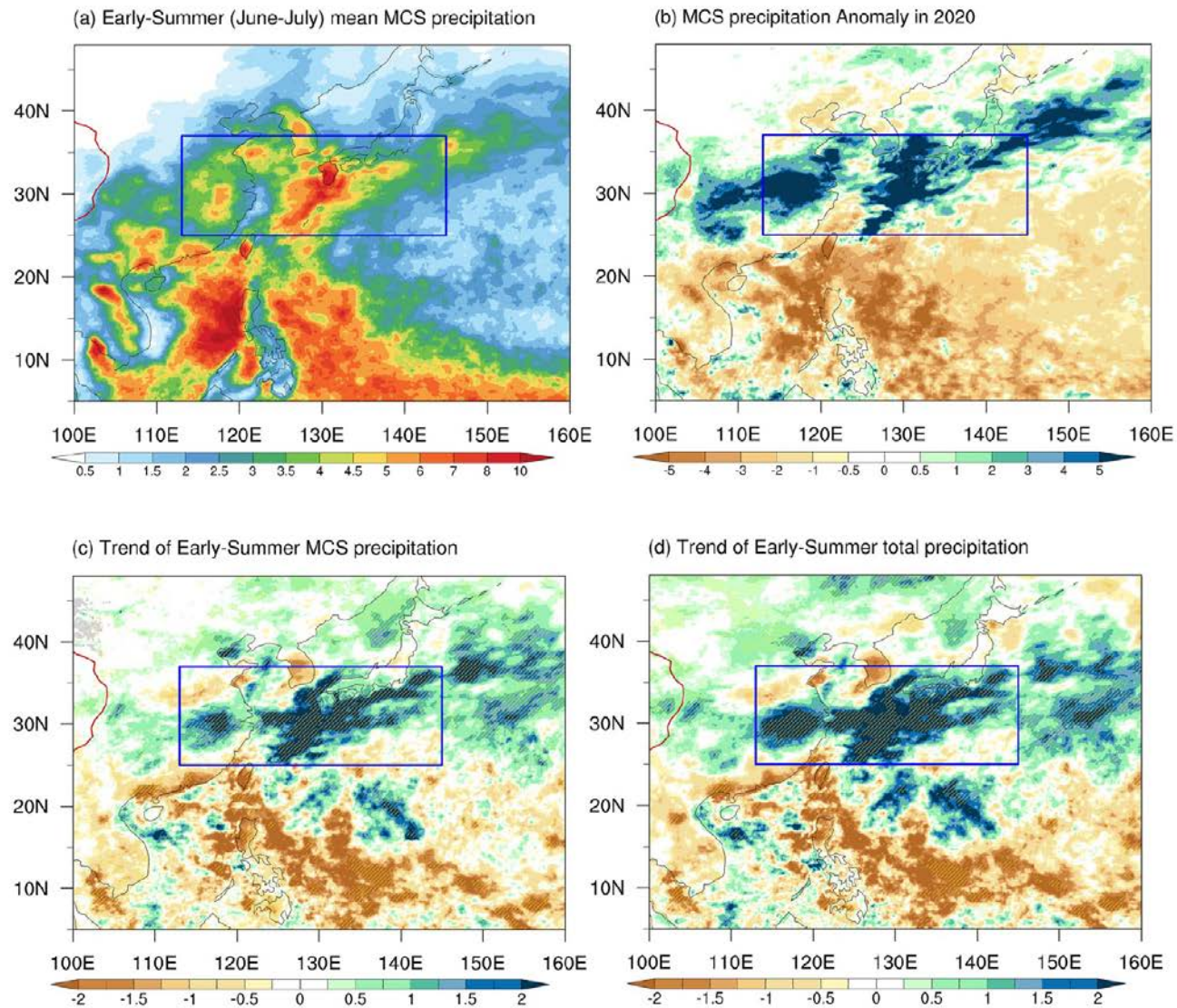
Figure 1. Mesoscale convective systems (MCSs) contributed the majority of the increasing trend of total precipitation in early summer over East Asia during the past two decades (from 2000 to 2021). (a) Early-summer MCS precipitation climatology (unit: mm day^{-1}). (b) Early-summer MCS precipitation anomalies in 2020 (unit: mm day^{-1}). (c) The MCS precipitation trend during the past two decades (unit: mm day^{-1} decade^{-1}). (d) The same as (c), but for the total precipitation trend. Grid points with a statistical significance exceeding the 95% confidence level (with a two-tailed Student's *t*-test) are marked by yellow diagonal lines. The red contour indicates the Tibetan Plateau (the topography exceeds 2,700 m). The blue boxes indicate the target domain (the East Asian rainband), where the statistical analyses have been performed.
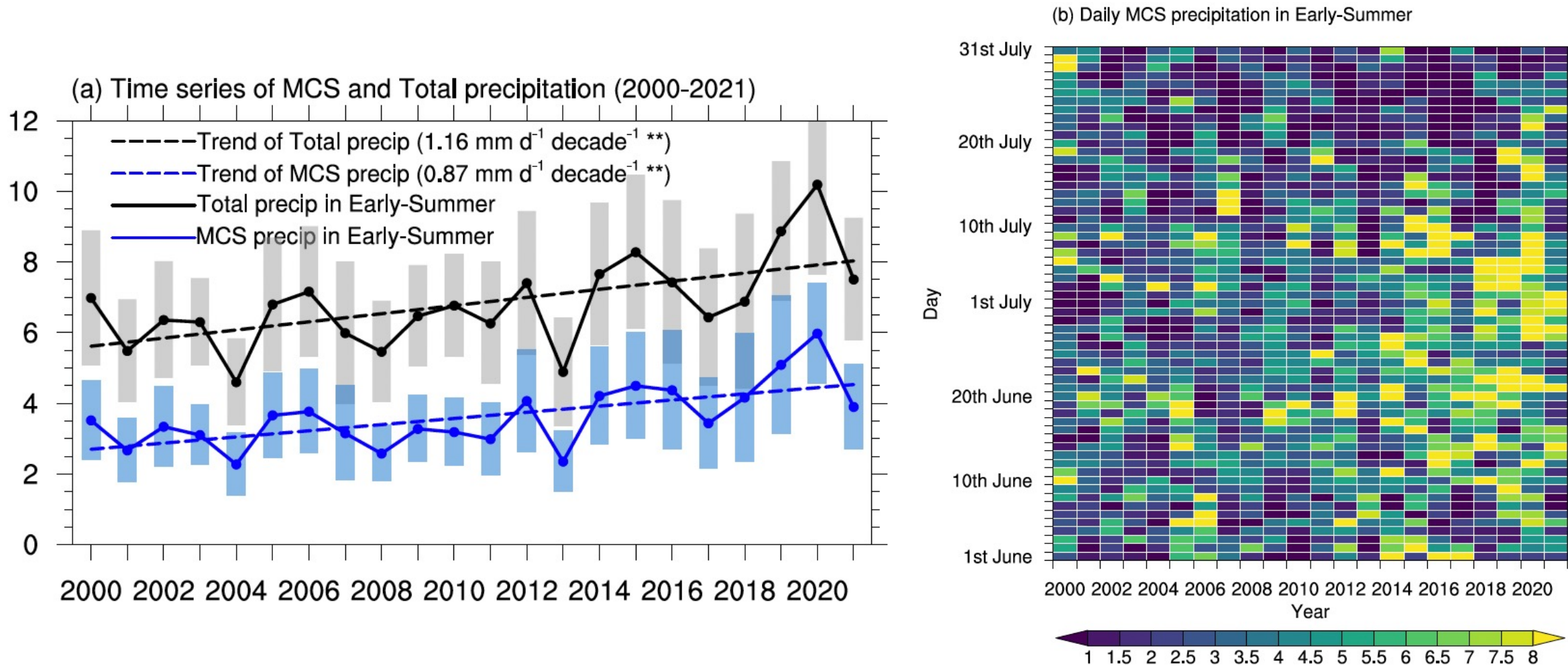
Figure 2. Time series and linear trends of MCS and total precipitation, and daily mean MCS precipitation within each early-summer season over the East Asian rainband. (a) Time series of early-summer MCS (blue) and total (black) precipitation (unit: mm day^{-1}), and linear trends of MCS (blue dashed line) and total precipitation (black dashed line; both statistically significant at 99% with two-tailed Student's t-tests) of early summer (unit: mm day^{-1} decade^{-1}). Here the gray/blue shadings represent the ± 0.5 standard deviations of the daily total/MCS precipitation in each early-summer. (b) Daily mean MCS precipitation (unit: mm day^{-1}) within each early-summer season during the past two decades (2000–2021).
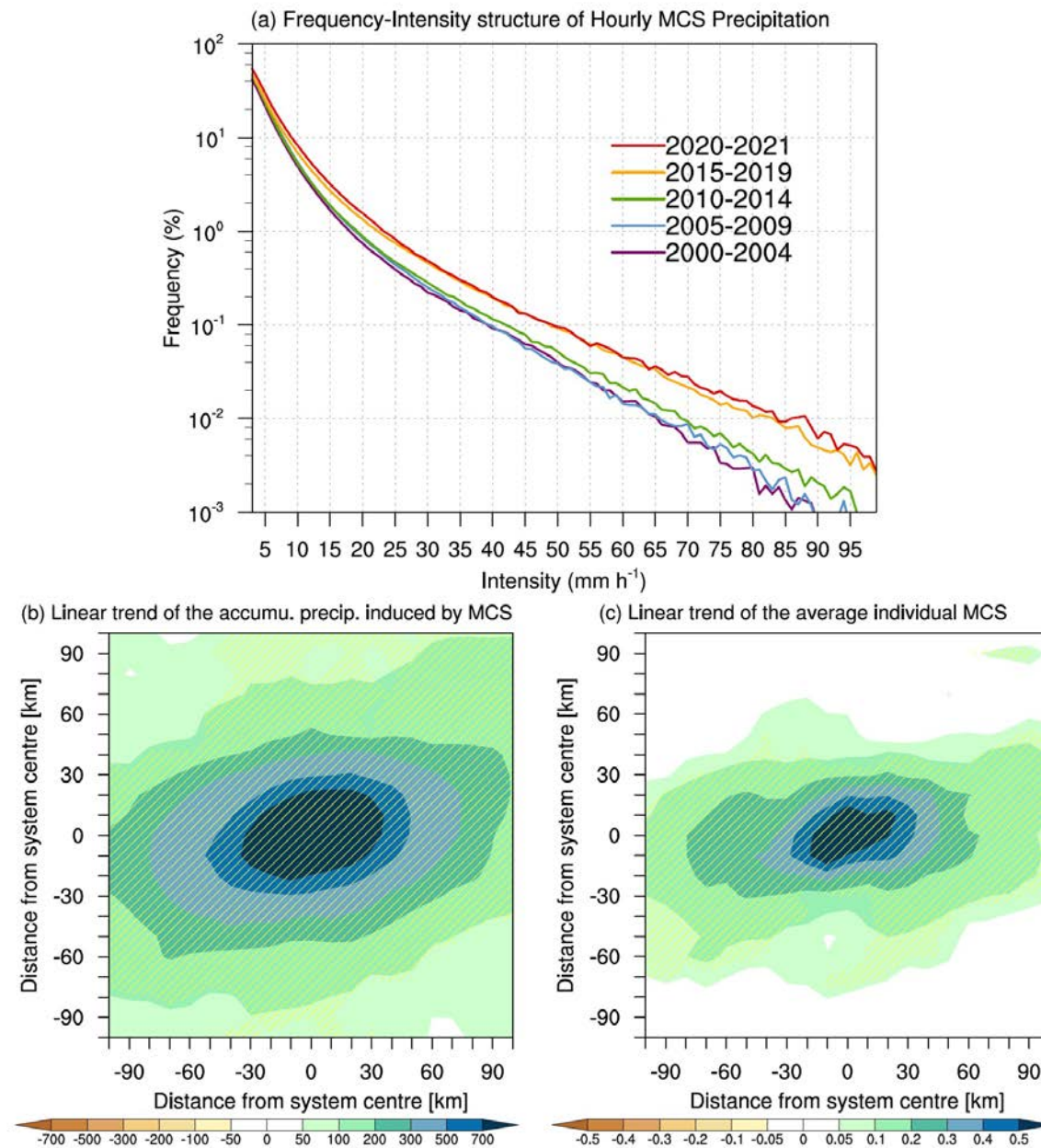
Figure 3. Probability density function of MCS hourly precipitation, and linear trends of the accumulated amount and the composited precipitation averages according to the location of the MCS precipitation center. (a) Frequency-Intensity structure of MCS hourly precipitation over the East Asian rainband. Linear trends of the (b) composited accumulated rainfall amount (unit: mm decade^{-1}) produced by all MCS and (c) hourly precipitation averages of each individual MCS (unit: mm h^{-1} decade^{-1}) in each early-summer season from 2000 to 2021. Grid points with a statistical significance exceeding the 95% confidence level are marked by yellow diagonal lines, with two-tailed Student's t-tests.
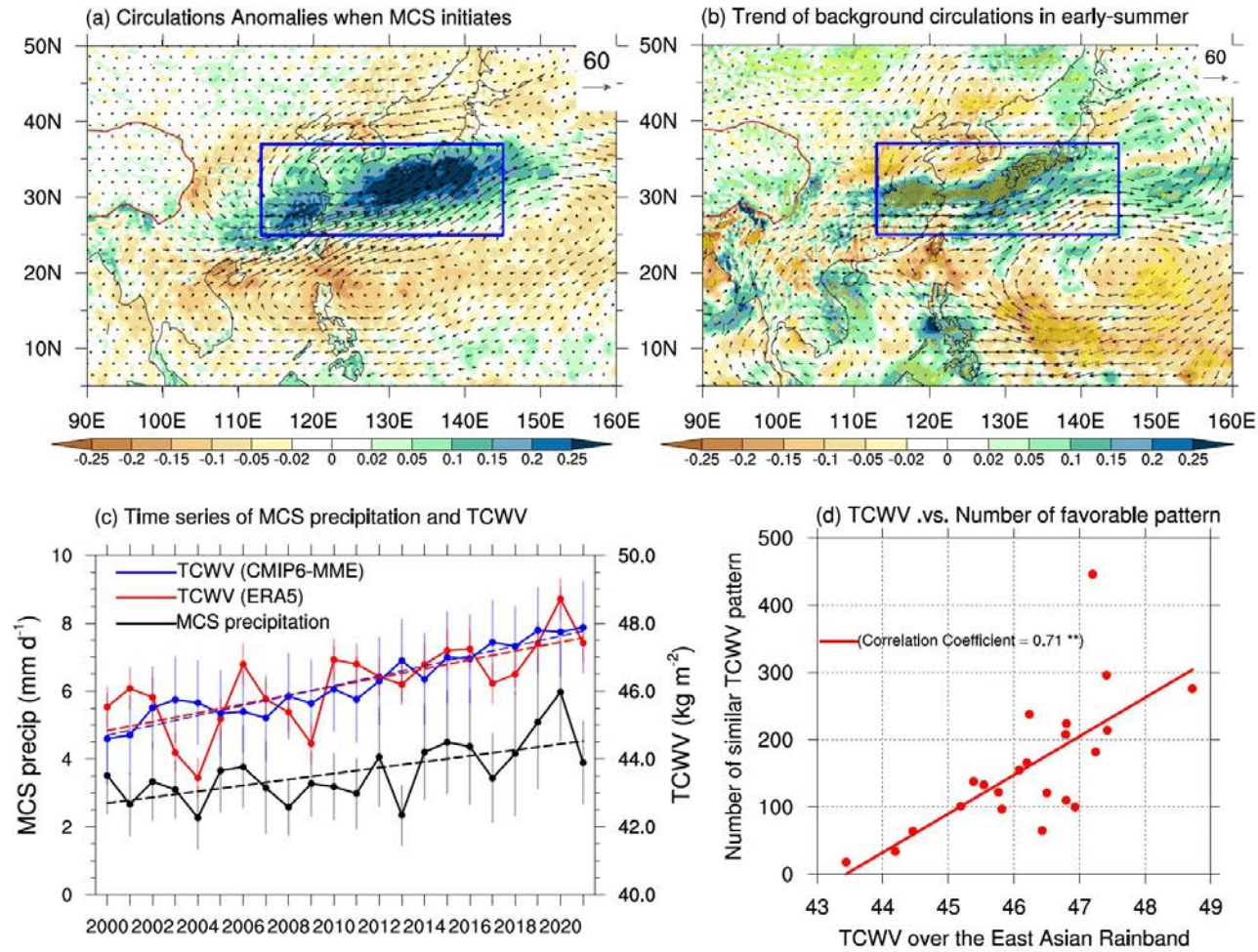
Figure 4. Large-scale environment anomalies when MCSs initiate over the East Asian rainband and changes of atmospheric circulations in the early-summer season during the last two decades. (a) The composited circulation anomalies when MCSs initiate compared to the early-summer climatology. The integrated water vapor transport and its convergence are indicated by the vectors (unit: kg m^{-1} s^{-1}) and shadings (unit: 10^{-4} kg m^{-2} s^{-1}), respectively. (b) The linear trends of the early-summer mean integrated water vapor transport (unit: kg m^{-1} s^{-1} decade^{-1}) and its convergence (unit: 10^{-4} kg m^{-2} s^{-1} decade^{-1}). Grid points with a statistical significance exceeding the 95% confidence level (with two-tailed Student's t-tests) are marked by yellow diagonal lines. The red contour indicates the Tibetan Plateau (the topography exceeds 2700 m). (c) Time series and linear trends of TCWV (unit: kg m^{-2}) in ERA5 reanalysis (red) and CMIP6 multi-model ensemble mean (MME; blue), and MCS precipitation (unit: mm day^{-1}; black) over the East Asian rainband (indicated by the blue box). The linear trends of TCWV and MCS precipitation are all statistically significant at 99% with two-tailed Student's t-tests. Here the gray/red bars represent the ±0.5 standard deviation of the daily precipitation/TCWV in each early summer. The blue bars indicate the ±0.5 standard deviation of the 25 CMIP6 models to represent the inter-model spread. (d) The relationship between the early-summer mean TCWV over the East Asian rainband (unit: kg m^{-2}) and the number of similar hourly TCWV patterns in each year during 2000–2021.